Received: 18 June 2025 | Revised: 20 September 2025 | Accepted: 6 October 2025

DOI: 10.1002/aic.70105

RESEARCH ARTICLE

Process Systems Engineering

AIChE JOURNAL

Model predictive control of an experimental protonic membrane steam methane reforming system

Dominic Peters[1] | Xiaodong Cui[1] | Yifei Wang[1] | Carlos G. Morales-Guio[1] | Panagiotis D. Christofides[1,2]

[1]Department of Chemical and Biomolecular Engineering, University of California, Los Angeles, California, USA

[2]Department of Electrical and Computer Engineering, University of California, Los Angeles, California, USA

Correspondence
Carlos G. Morales-Guio and Panagiotis D. Christofides, Department of Chemical and Biomolecular Engineering, University of California, Los Angeles, CA, USA.
Email: moralesguio@g.ucla.edu; pdc@seas.ucla.edu

Funding information
U.S. Department of Energy, Grant/Award Number: DE-EE0007613

Abstract

The automation and control of protonic membrane reformers can facilitate the commercialization of this emerging hydrogen-producing technology. To this end, a decentralized and offset-free model predictive control (MPC) approach is developed to explore potential automation pathways for a protonic membrane reforming system that achieves 84% hydrogen recovery at 0.69 A·cm^{-2} (15.2 cm^2 active surface area). Three physics-based and data-driven models estimate thermal hydrogen generation on the anode, electrochemical hydrogen recovery on the cathode, and steam generation. During setpoint tracking, the experimental results of the MPC architecture show faster hydrogen purification rate settling times and implementable control action profiles between sampling times, protecting the actuators and the thermo-electrochemical performance of the protonic membrane. Ultimately, this work points to control strategies for protonic membrane systems that incorporate a combination of classical and predictive controllers with disturbance-observer-based error quantification for optimal hydrogen production.

KEYWORDS
disturbance observer (DOB), model predictive control (MPC), process systems engineering, protonic membrane reformer (PMR), steam methane reforming (SMR)

1 | INTRODUCTION

Steam methane reforming (SMR) is a chemical process that generates 95% of the hydrogen circulating in the world economy.[1] Conventional steam methane reforming plants are designed with a series of fired reformers, shift reactors, and separation units to generate and purify hydrogen from natural gas. Although these types of plants have been operated for more than 80 years and are highly optimized chemical production processes, there is a growing interest in transitioning to electrified furnace reactors, as furnace units consume the largest fraction of process energy in SMR plants.[2] Electric power may also be used in state-of-the-art reformer designs to facilitate hydrogen transport across ion-conducting ceramic membranes. The benefit of using ion-conducting membranes for methane reforming, herein referred to as protonic membrane reformers (PMR), is the removal of hydrogen from thermal reaction zones by way of electrochemical separation in a single reactor-separator unit. As a result, a thermodynamic equilibrium shift increases hydrogen production rates in reaction zones that lower the operating temperatures of protonic membrane reformers by at least 100°C, compared to conventional steam methane reformers. However, full heat integration and automation of PMR systems are the two primary bottlenecks currently inhibiting the commercialization of ion-conducting hydrogen generators, as discussed, e.g., by Fjeld et al.[3]

At a conceptual level, protonic membrane reformers are a special case of emerging SMR energy technologies that drive

Dominic Peters and Xiaodong Cui contributed equally to this work.

thermo-electrochemical reactions for hydrogen compression and purification in a single chemical processing unit; in this design, the water-gas shift (WGS) reactors and pressure-swing adsorption units of conventional hydrogen plants are foregone. The dependence of thermal reactions on electrochemical hydrogen separation rates, protonic membrane reformer temperatures, feed stream steam-to-carbon (S/C) ratios, and membrane conductivity inevitably leads to nonlinear process dynamics and multivariable couplings. Further, the feed steam-to-carbon ratio is inherently linked to both thermal reaction rates and the anode steam partial pressure. These factors determine the protonic membrane separation performance, leading to input-output variable interactions between the main thermo-electrochemical subprocesses of reaction, transport, and separation. Therefore, we must address the challenge of developing robust and stable predictive control architectures for PMR systems, since the application of nonlinear model predictive control algorithms to multi-time-scale systems with uncertain disturbance phenomena often leads to controller ineffectiveness and closed-loop instabilities.[4]

A body of chemical engineering literature has evaluated different control methodologies for experimental hydrocarbon reformers and proton exchange membrane fuel cells. Selected works are provided in Table 1, but validated dynamic models and experimental applications of process control for protonic membrane reformers remain unreported. Therefore, this work seeks to establish advanced automation pathways that can withstand the stochastic disturbance phenomena that may arise in such systems. Specifically, membrane conductivity, local anode dehydration, hydrogen depletion,[11,12] catalyst deactivation, and pressure oscillations are all uncertain physical factors that occur during regular operation and must be overcome by robust feedback controller designs.

To that end, state observers have often been used in industrial control algorithms to estimate unmeasured states, filter noise, and quantify disturbance-based errors. Disturbance observers are a subset of state observers that are often programmed within MPC algorithms to achieve controller robustness in systems subject to estimation uncertainties and external disturbance phenomena.[13] In view of this, the first decentralized model predictive control (DMPC) architecture to regulate the steam-to-carbon ratio of reactants, hydrogen purification rates, and the overall rate of hydrogen generation is developed in the present work for a 15.2 cm^2 protonic membrane that has been integrated into a reforming system. An offset-free disturbance observer is also used to mitigate plant-model mismatch in the hydrogen generation rate control loop by adapting a reaction engineering model to shifts in catalytic activity, cell voltage spikes, local dehydration of membrane surfaces, and sensor drift. The transient responses of all controlled variables were previously captured in validated models constructed by Cui et al.,[14] and are now subsequently implemented in three experimental predictive controllers subject to the aforementioned experimental disturbance phenomena.

Compared to a classical multi-input multi-output control scheme, the DMPC architecture for hydrogen purification demonstrates an improved time-to-setpoint, an improved adherence to process-specific constraints, and enhanced recovery rates exceeding 84%. Furthermore, setpoint dynamic compensation of the hydrogen purification rate prevents hydrogen depletion at the protonic membrane anode, helping to limit carbon formation reactions and voltage spikes. Near-complete methane conversion at reformer temperatures below 800°C is also observed. Overall, these experiments contribute to the science of scale-up[15] and reaction engineering[16] by quantifying the extent of multivariable couplings in dynamically-operated thermo-electrochemical systems to provide potential automation pathways and enable optimal control of PMR systems.

2 | PRELIMINARIES

2.1 | Notation

The symbol $\|\cdot\|$ represents the Euclidean norm of a vector. $\mathbb{R}$ represents the set of real numbers.

2.1.1 | Definitions of variables used in the modeling of the reactor and bubbler

- $A_h^{a,PMR}$, $A_h^{c,PMR}$: Surface area for heat loss, of PMR anode, of PMR cathode [m^2].

TABLE 1 Summary of literature on control strategies for reforming systems (selected papers).

Authors	System	Control strategy	Main contribution
Lin et al. (2006)[5]	Methane reformer simulation based on empirical data	SISO MPC	PI control of hydrogen production via methane feed flow rate
Malik et al. (2020)[6]	Autothermal reformer with PEMFC simulation	Classical MIMO	PI and PID control of temperature and hydrogen flow rate using furnace heat and PEMFC current
Cifuentes et al. (2023)[7]	Experimental high-pressure methanol reformer	Classical SISO	Experimental PI control of hydrogen production via methanol feed flow rate at 12 bar
Andreasen et al. (2013)[8]	Experimental methanol reformer	Classical MIMO	Two PI temperature controllers
Li et al. (2022)[9]	Low-temperature PEMFC	SISO MPC	Experimental MPC for controlling PEMFC temperature
Citmaci et al. (2024)[10]	Experimental electrified methane reformer	SISO MPC	MPC with extended Luenberger observer for hydrogen production control

- A_i: Pre-exponential factor of adsorption constant K_i [Pa^{-1} for $i = CH_4, H_2, CO$ and unitless for $i = H_2O$].
- A_j: Pre-exponential factor of rate coefficient k_i [$mol \cdot Pa^{0.5} \cdot (kg_{cat} \cdot s)^{-1}$ for $j = 1$ (SMR reaction), $mol \cdot (Pa \cdot kg_{cat} \cdot s)^{-1}$ for $j = 2$ (WGS reaction)].
- $C_i^{a,PMR}$, $C_i^{c,PMR}$: Concentration of gas i, in PMR anode chamber, in PMR cathode chamber [$mol \cdot m^{-3}$].
- $C_{p,i}$: Heat capacity of species i [$J \cdot (kg \cdot K)^{-1}$].
- E_j: Activation energy of reaction j [$J \cdot mol^{-1}$].
- $F_{i,0}^{a,PMR}$, $F_{i,0}^{c,PMR}$: Inlet molar flow rate of gas i in PMR anode chamber, in PMR cathode chamber [$mol \cdot s^{-1}$].
- $F_{k,ex}$: Extraction rate of gas k [$mol \cdot s^{-1}$].
- I_m, I_f: Current through membrane, current to heat furnace [A].
- K_i: Adsorption constant of gas i [Pa^{-1} for $i = CH_4, H_2, CO$ and unitless for $i = H_2O$]
- K_j: Equilibrium constant of reaction j [Pa^2 for $j = 1$ (SMR reaction), unitless for j =2 (WGS reaction)]
- k_j: Reaction rate constant of reaction j [$mol \cdot Pa^{0.5} \cdot (kg_{cat} \cdot s)^{-1}$ for $j = 1$ (SMR reaction), $mol \cdot (Pa \cdot kg_{cat} \cdot s)^{-1}$ for $j = 2$ (WGS reaction)]
- $P^{a,PMR}$, $P^{c,PMR}$: Pressure of PMR anode chamber, of PMR cathode chamber [Pa]
- $q^{a,PMR}$, $q^{c,PMR}$: Outlet volumetric flow rate of PMR anode chamber, of PMR cathode chamber [$m^3 \cdot s^{-1}$].
- r_j: Rate of reaction j per kilogram of catalyst [$mol \cdot (kg \cdot s)^{-1}$].
- R: Universal gas constant [$J \cdot (mol \cdot K)^{-1}$].
- R_f, R_m: Electric resistance of furnace, of membrane [Ω].
- T^a, $T^{a,PMR}$, $T^{c,PMR}$: Temperature of ambient, of PMR anode chamber, of PMR cathode chamber [K].
- $T_0^{a,PMR}$, $T_0^{c,PMR}$, T_0^b: Temperature at the inlet of PMR anode chamber, of PMR cathode chamber [K].
- $U_h^{a,PMR}$, $U_h^{c,PMR}$: Overall heat transfer coefficient of PMR anode chamber, of PMR cathode chamber [$J \cdot (s \cdot K \cdot m^2)^{-1}$].
- $V^{a,PMR}$, $V^{c,PMR}$: Volume of PMR anode chamber, of PMR cathode chamber [m^3].
- W_{cat}: Weight of catalyst [kg].
- ΔH_{r_j}: Enthalpy change of reaction j [$J \cdot mol^{-1}$].
- $\rho_i^{a,PMR}$, $\rho_i^{c,PMR}$: Density of species i of PMR anode chamber, of PMR cathode chamber [$kg \cdot m^{-3}$].

2.2 | Protonic membrane reforming system

The objective of the PMR operation is to generate a purified hydrogen product stream from methane and steam. The system accomplishes hydrogen purification by catalyzing thermo-electrochemical reactions, separations, and compression under applied thermal and electrical energy inputs. To properly define and formulate the control problem, the mass and energy dynamics of the control volumes that comprise the PMR system are considered. There are four primary control volumes where dynamic mass and energy exchanges occur: The anodic and cathodic bubblers, the anode chamber, and the cathode chamber. The BZCY ($BaZrCeYO_{3-\delta}$) protonic membrane in Figure 1A is the interface where thermo-electrochemical reactions convert methane to hydrogen, create carbon oxide by-products, and drive the purification of hydrogen. Figure 2 highlights key processing units, sensors, and actuators for the experimental PMR system. A detailed discussion on the inner workings, hardware factors, and chemical physics of the protonic membrane and general PMR system is provided in previous works.[3,17,18]

The anodic feed stream of the PMR unit is a mixture of steam, methane, hydrogen, and trace argon. The cathodic feed stream contains pure hydrogen, which is used as a sweep gas to transport purified hydrogen to the cathodic outlet of the PMR system. Within the protonic membrane anode chamber, steam methane reforming and water-gas shift reactions are catalyzed at the anode surface by a metallic nickel dispersion on a barium-zirconate ceramic. Under an applied electric current, hydrogen oxidation also occurs at the anode surface. The resulting protons migrate across the ceramic electrolyte to the cathode, where hydrogen evolution produces hydrogen gas molecules. The endothermic steam methane reforming reaction and exothermic water-gas shift reaction induce a nonlinear temperature gradient in both time and space within the PMR unit. To generate

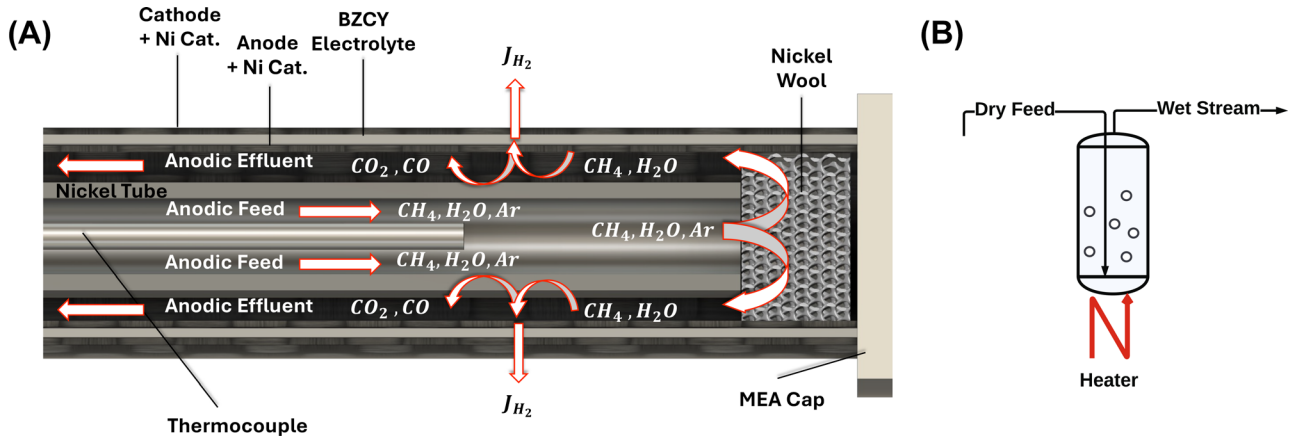

FIGURE 1 Process schematics of the (A) PMR and (B) bubbler units, highlighting the feed flow paths and physical/thermo-electrochemical transformation zones.

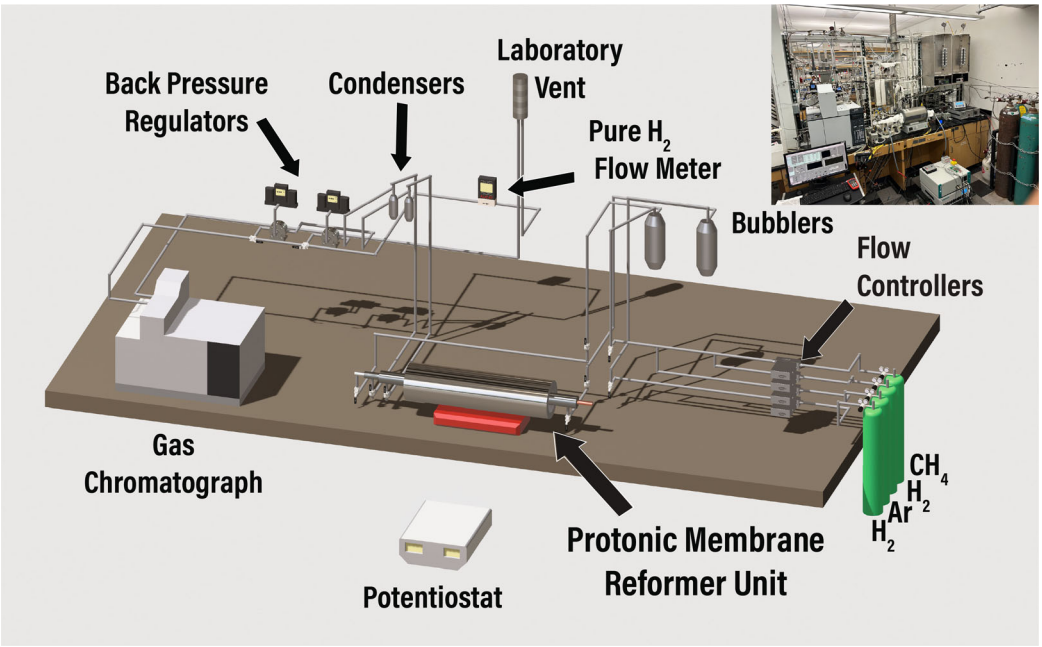

FIGURE 2 Overview of primary PMR system components and sensors.

steam for the thermo-electrochemical reactions, bubbler units are used (Figure 1B). The steam generation rate in the bubblers is a function of the partial pressure of steam and the total feed flow rate of carrier gas species.[19] Field temperature controllers are installed in the housing of the bubblers to regulate the internal liquid temperature via classical (proportional-derivative) control closed-loops.

Experimental control in these subsystem units requires online sensors for temperature, pressure, and gas composition measurements. Figure 3 provides a detailed piping and instrumentation diagram of the electronic devices used to record, transmit, or activate changes in process variables from a custom LabVIEW interface run on the main computational processor. The relevant process sensors for the MPC architecture studied in this work are the anodic bubbler thermocouple, anodic bubbler pressure transducer, anode chamber thermocouple, anode chamber pressure transducer, anodic effluent gas chromatogram, and a digital mass flow meter to quantify cathodic products. From the digitized electrical signals of these transmitters, the required thermodynamic states of the system are recorded at specified sampling rates. Online recording of the system states enables the quantification of disturbance phenomena to augment the state estimation model and improve the performance of the decentralized predictive controllers over the entire control action window.

2.3 | Thermal reaction kinetics

Steam methane reforming and water-gas shift thermal reactions:

$$CH_4 + H_2O \rightleftharpoons CO + 3H_2 \quad \Delta H_{298K} = +206\,\text{kJ/mol} \tag{1a}$$

$$CO + H_2O \rightleftharpoons CO_2 + H_2 \quad \Delta H_{298K} = -41\,\text{kJ/mol} \tag{1b}$$

A Langmuir-Hinshelwood-Hougen-Watson (LHHW) chemical kinetics mechanism for heterogeneous catalysis of hydrocarbons on active metals is routinely applied to steam methane and protonic membrane reformers in chemical engineering literature.[20] The mechanism combines power-law and thermodynamic equilibrium analysis with microkinetic parameters that incorporate the competitive adsorption-desorption of chemical species on available reactive sites.[21] To apply the LHHW mechanism, the standard assumptions are a kinetic-limited operating regime, uniform pressure in the anode chamber, well-dispersed surface sites along the Ni-BZCY anode surface, and uniform kinetic activity among all catalytic surface sites. The overall kinetic rate equations via the LHHW mechanism for the SMR and WGS reactions are:

$$r_1 = \frac{k_1}{P_{H_2}^{2.5}} \frac{P_{CH_4}P_{H_2O} - \frac{P_{H_2}^3 P_{CO}}{K_{EQ1}}}{(DEN)^2} \tag{2a}$$

$$r_2 = \frac{k_2}{P_{H_2}} \frac{P_{CO}P_{H_2O} - \frac{P_{H_2}P_{CO_2}}{K_{EQ2}}}{(DEN)^2} \tag{2b}$$

$$DEN = 1 + K_{CO}P_{CO} + K_{H_2}P_{H_2} + K_{CH_4}P_{CH_4} + K_{H_2O}\frac{P_{H_2O}}{P_{H_2}} \tag{2c}$$

with r_1 and r_2 capturing the overall kinetic rates for the SMR (Equation 1a) and WGS (Equation 1b) catalytic reactions, respectively. In the relation, k_1 and k_2 are the forward reaction rate constants, K_{EQ1}

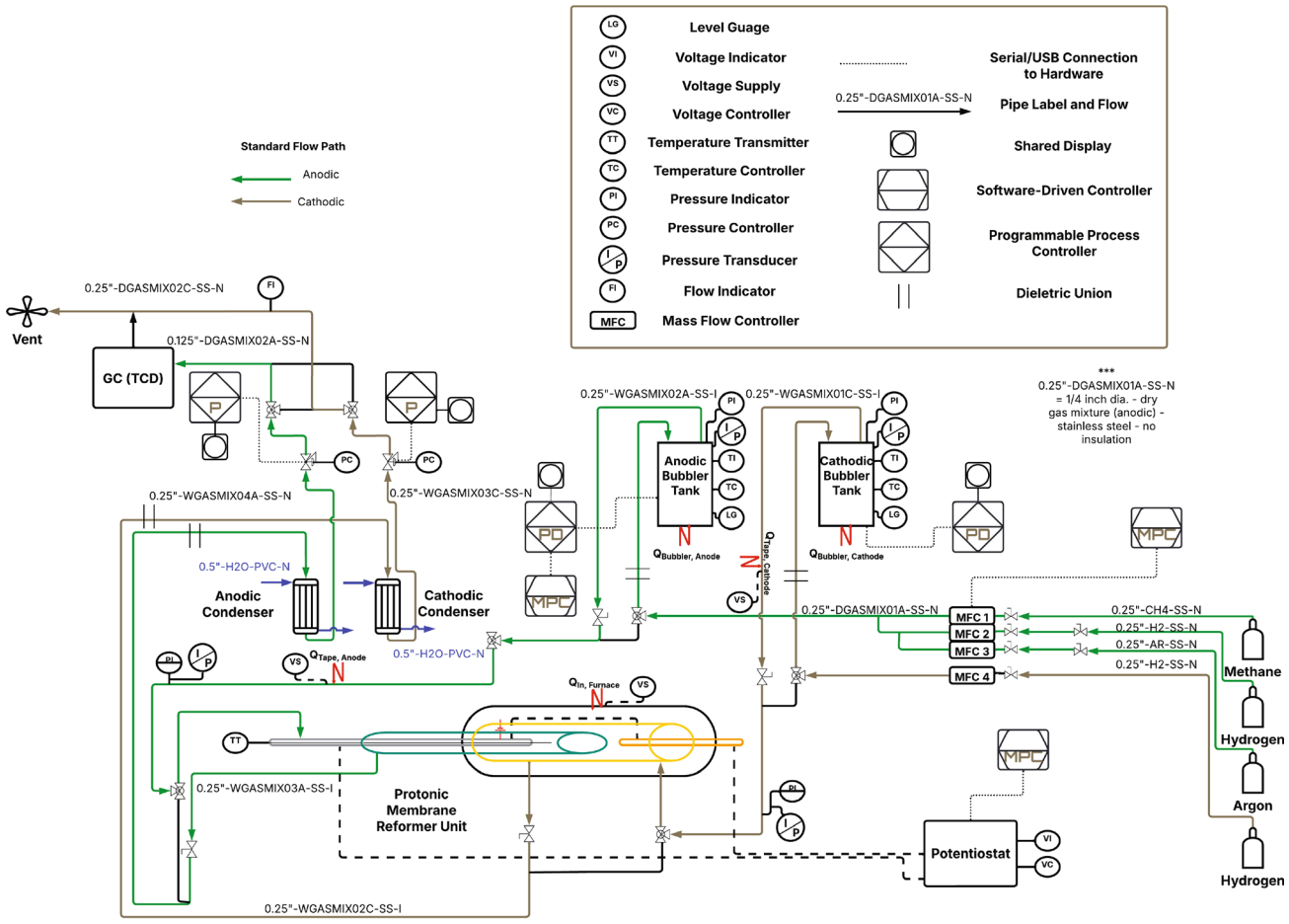

FIGURE 3 System P&ID—piping flow paths, piping dimensions, chemical processing units, actuators, sensors, controllers, and electrical pathways.

and K_{EQ2} are equilibrium constants, *DEN* is the denominator term derived from the microkinetic surface site mechanism for catalyst adsorption-desorption constants, and P_i are the partial pressures of reactants and products. In Equation (2c), K_i, for $i = CO, H_2, CH_4, H_2O$, is the adsorption coefficient of each species on nickel catalyst sites. Rate constants and adsorption coefficients in Equation (2) follow an Arrhenius dependence as a function of the reformer temperature:

$$k_j = A_j \exp\left(-\frac{E_j}{RT}\right), \quad j = 1,2 \tag{3a}$$

$$K_i = A_i \exp\left(-\frac{\Delta H_i}{RT}\right), \quad i = CH_4, H_2O, CO, H_2 \tag{3b}$$

Listed in Table 2 are the parameters used to calculate the thermal reaction kinetics at each time step in the reaction engineering model developed in Section 2.6. The reference temperature for k_i, K_{CO}, and K_{H_2} is 648 K when computing the van't Hoff equation for rate constants and absorption coefficients. K_{CH_4} and K_{H_2O} are calculated from a reference temperature of 823 K. Methane conversion, as a result of the forward progression of the SMR reaction, is quantified in Equation (4):

$$X_{CH_4} = 1 - \frac{F_{CH_4}^{a,PMR}}{F_{CH_4,0}^{a,PMR}} \tag{4}$$

where methane conversion X_{CH_4} is a function of the ratio of methane at the feed $F_{CH_4,0}^{a,PMR}$ and outlet $F_{CH_4}^{a,PMR}$ of the protonic membrane reformer.

2.4 | Electrochemical reaction-separation term

Protonic membrane reformers drive the separation of hydrogen from the anode surface, through the solid BZCY electrolyte, and to the cathode surface by way of hydrogen oxidation and reduction (HER/HOR) electrochemical reactions, defined in Equation (5):

$$H_2 \rightleftharpoons 2H^+ + 2e^- \quad E^\circ = 0.00\,\text{V (vs. SHE)} \tag{5}$$

Hydrogen is oxidized at nickel surface sites on the anode, which forms two protons that migrate through the membrane for every molecule of hydrogen that reacts. At the cathode surface, HER reduces these protons back into hydrogen gas molecules.[17] The electrical input energy to HER/HOR reactions is supplied by a potentiostat. To

TABLE 2 Kinetic parameters from Xu and Froment.[22]

Parameter		Value	Unit
P_{ref}	=	1.01	bar
E_1	=	240.1	kJ·mol^{-1}
E_2	=	67.13	kJ·mol^{-1}
A_1	=	4.225×10^{15}	kmol·bar$^{0.5}$·(kg$_{cat}$·hr)$^{-1}$
A_2	=	1.955×10^{6}	kmol·(kg· bar·hr)$^{-1}$
K_{EQ1}	=	1.198×10^{13}	bar^2
K_{EQ2}	=	1.767×10^{-2}	–
A_{CO}	=	8.23×10^{-5}	bar^{-1}
A_{H_2}	=	6.12×10^{-9}	bar^{-1}
A_{CH_4}	=	6.65×10^{-4}	bar^{-1}
A_{H_2O}	=	1.77×10^{5}	–
ΔH_{CO}	=	−70.65	kJ·mol^{-1}
ΔH_{H_2}	=	−82.9	kJ·mol^{-1}
ΔH_{CH_4}	=	−38.28	kJ·mol^{-1}
ΔH_{H_2O}	=	88.68	kJ·mol^{-1}
W_{cat}	=	1.3×10^{-5}	kg

Note: W_{cat} is a fitting parameter used to match the observed experimental reaction kinetics to the LHHW kinetic model; W_{cat} is not a Xu and Froment parameter.

account for hydrogen generation, consumption, and separation in the anode and cathode reformer chambers, a separation constant is developed that is a function of the applied electric current to the protonic membrane. Specifically, the electrokinetic rate of reaction is directly correlated to the electron balance across the protonic membrane cell of the reformer unit,[23] presented as Equation (6):

$$n_e F_{H_2,ex} F = \eta_F I_m \tag{6}$$

where n_e represents the moles of electrons transferred per mole of removed hydrogen, $n_e = 2$ (Equation 5), F is Faraday's constant, and η_F is the Faradaic efficiency. In this case, a 100% Faradaic efficiency is assumed based on protonic membrane separations data provided in Fjeld et al.[3] and control experiments in our laboratory (*vide infra*). That is to say, 100% of the applied current to the protonic membrane goes towards electrochemical separation reactions in the studied reaction-separation unit. This is because the electrochemical oxidation and production of hydrogen are facile on Ni catalysts, and there are no parasitic side reactions that could result in the loss of electrons under the tested conditions. After rearranging Equation (6) and incorporating this assumption, the hydrogen extraction rate from the anode chamber can be expressed as Equation (7).

$$F_{H_2,ex} = \frac{I_m}{2F} \tag{7}$$

A key metric for establishing the thermo-electrochemical performance of the protonic membrane is the hydrogen recovery ratio, which is the ratio of electrochemically purified hydrogen to the overall hydrogen generated from thermal catalysis at the anode surface of the membrane. This ratio is provided in Equation (8):

$$HR = \frac{F_{H_2,ex} \cdot 100\%}{F_{H_2,ex} + F_{H_2}^{a,PMR} - F_{H_2,0}^{a,PMR}} \tag{8}$$

where the hydrogen recovery percentage HR is the fraction of hydrogen extracted from anode to cathode $F_{H_2,ex}$ in reference to the total amount of hydrogen generated from the SMR and WGS reactions. To quantify the total amount of hydrogen produced from thermal catalysis, the feed hygroden $F_{H_2,0}^{a,PMR}$ is subtracted from the extracted hydrogen and the anodic effluent hydrogen $F_{H_2}^{a,PMR}$.

2.5 | Anodic steam bubbler dynamic model

The anodic bubbler in the PMR system generates steam for the SMR reactions and hydrates the protonic membrane for enhanced ion conductivity. In Cui et al.,[14] a first-principles model was developed based on the mass and energy balances of the anodic bubbler for which the heat supplied to the bubbler Q_b determines the bubbler temperature and steam generation rate. However, in the experimental system, a field PD-controller (proportional-derivative controller) regulates the bubbler temperature by modulating the voltage supplied to the electrical heating tape that encapsulates the bubbler unit. Energy from the tape is transferred to a water reservoir housed within the stainless steel bubbler cylinder. To determine the states of the bubbler process in real-time, a second-order process model is constructed from open-loop experiments. This model captures the approximate inertial and damping effects of PD-control on the anodic bubbler energy dynamics, defined here as:

$$X_b(s) = \frac{k_{p,b} U(s)}{\tau_b^2 s^2 + 2\zeta_b \tau_b s + 1} \tag{9}$$

where $k_{p,b}$, τ_b, and ζ_b are constant parameters for the bubbler process gain, the time constant of bubbler dynamics, and the damping coefficient of the second-order model, respectively. This equation can be transformed into two first-order ordinary differential equations in the time domain:

$$\dot{x}_{1b} = x_{2b} \tag{10a}$$

$$\dot{x}_{2b} = \frac{1}{\tau_b^2}\left(k_{p,b} u_b - 2\zeta_b \tau_b x_{2b} - x_{1b}\right) \tag{10b}$$

where x_{1b} is the output state of the bubbler and x_{2b} is the rate of change of the output state. The output state refers to the true bubbler temperature measured by an internal thermocouple. T_{sp} is the manipulated variable input of the field PD-controller, defined as u_b in Equation (10). Adjustable parameters $k_{p,b}$ and τ_b are incorporated in the second-order model to tune the process gain and time constant to match the real dynamics of the anodic bubbler.

2.6 | Lumped-parameter reformer model

A nonisothermal lumped-parameter framework is used as the primary reformer model (Figure 4). A secondary model for electrochemical hydrogen separation (Equation 7) is incorporated into the design equations to approximate mass and energy transport within the PMR unit. The lumped-parameter design equations assume perfect mixing, uniform mass and energy distributions, and a uniformly dispersed catalyst for homogeneous reaction rates. In addition, a constant density of the gas phase is assumed spatially but not temporally, given the dependence of gas-phase densities on temperature and pressure. A constant pressure is also assumed, and species mole balances for each gas-phase reactant and product in the anode chamber follow the general form:

$$\dot{C}^{a,PMR} = \frac{\boldsymbol{F}_0^{a,PMR} + \boldsymbol{R} - q^{a,PMR}\,\boldsymbol{C}^{a,PMR} - \boldsymbol{F}_{ex}}{V^{a,PMR}} \tag{11a}$$

$$\boldsymbol{C}^{a,PMR} = \begin{bmatrix} C_{CH_4}^{a,PMR} \\ C_{H_2O}^{a,PMR} \\ C_{CO}^{a,PMR} \\ C_{H_2}^{a,PMR} \\ C_{CO_2}^{a,PMR} \\ C_{Ar}^{a,PMR} \end{bmatrix}, \quad \boldsymbol{F}_0^{a,PMR} = \begin{bmatrix} F_{CH_4,0}^{a,PMR} \\ F_{H_2O,0}^{a,PMR} \\ F_{CO,0}^{a,PMR} \\ F_{H_2,0}^{a,PMR} \\ F_{CO_2,0}^{a,PMR} \\ F_{Ar,0}^{a,PMR} \end{bmatrix}, \quad \boldsymbol{R} = \begin{bmatrix} -r_1 W_{cat} \\ (-r_1 - r_2) W_{cat} \\ r_1 W_{cat} \\ (3r_1 + r_2) W_{cat} \\ -r_2 W_{cat} \\ 0 \end{bmatrix}, \quad \boldsymbol{F}_{ex} = \begin{bmatrix} 0 \\ 0 \\ 0 \\ \frac{I_m}{2F} \\ 0 \\ 0 \end{bmatrix} \tag{11b}$$

where $i = CH_4, H_2O, CO, H_2, CO_2, Ar$ and $\dot{C}_i^{a,PMR}$ is the rate of change in the molar concentration of anode species i contained in the vector $\boldsymbol{C}^{a,PMR}$. The ordinary differential equations relate the product of $\boldsymbol{C}^{a,PMR}$ and the anode chamber volume $V^{a,PMR}$ to a balance of the anodic feed flow rates of $\boldsymbol{F}_0^{a,PMR}$, the molar rates of reaction in $\boldsymbol{R}$, and the molar separation rate of hydrogen in $\boldsymbol{F}_{ex}$. For the energy balance, the electric furnace heat and Joule-heating from hydrogen separation are coupled with terms for external heat loss, enthalpies of reactions, and enthalpies of reacting and inert species. Considering these transport phenomena, the anode chamber energy balance is contained in the following equation:

$$\dot{T}^{a,PMR} = \frac{f_h^{a,PMR} I_f^2 R_f + \sum F_{i,0}^{a,PMR} \int_{T_0^{a,PMR}}^{T^{a,PMR}} C_{p,i}\, dT' - r_1 W_{cat} \Delta H_{r_1}(T^{a,PMR}) - r_2 W_{cat} \Delta H_{r_2}(T^{a,PMR})}{\sum \rho_i^{a,PMR} C_{p,i} V^{a,PMR}} + \frac{U_h^{a,PMR} A_h^{a,PMR} (T^a - T^{a,PMR}) + \frac{1}{2} I_m^2 R_m + \frac{I_m}{4F} RT^{a,PMR} \ln\left(\frac{P^{c,PMR}}{P^{a,PMR}}\right)}{\sum \rho_i^{a,PMR} C_{p,i} V^{a,PMR}} \tag{12}$$

where $i = CH_4, H_2O, CO, H_2, CO_2, Ar$ for the heat capacities $C_{p,i}$ of all gas species in the anode chamber and $\dot{T}^{a,PMR}$ forms the energy balance as the rate of change of temperature in the anode chamber. The fraction of furnace heat conducted through the anode chamber is represented by $f_h^{a,PMR}$. It is also assumed that the energy supplied to the membrane by Joule-heating is split evenly between the anode and cathode chambers of the PMR unit, hence the multiplication of the $I_m^2 R_m$ term by a factor of one-half. This assumption is confirmed by the experimental results presented in Section 4. The total volumetric flow rate through the anode chamber is calculated by combining the anodic energy balance with the ideal gas law, as follows:

$$q^{a,PMR} = \left(\sum_{i,0}^{a,PMR} F + 2 r_1 W_{cat} - \frac{I_m}{2F} \right) \frac{RT^{a,PMR}}{P^{a,PMR}} + \frac{V^{a,PMR}}{T^{a,PMR}} \dot{T}^{a,PMR} \tag{13}$$

where $q^{a,PMR}$ is the total volumetric flow rate in the anode chamber that evolves with time, temperature, methane conversion, anodic feed flow rates, and the hydrogen extraction rate into the cathode chamber. $P^{a,PMR}$ is the anode chamber pressure. On the opposing side of the protonic membrane is a cathode chamber where purified hydrogen is transported, compressed, and swept away by a wet hydrogen carrier stream. Only water vapor and hydrogen are contained within the cathodic streams of the system, and the design equation for the evolution of either species takes the form:

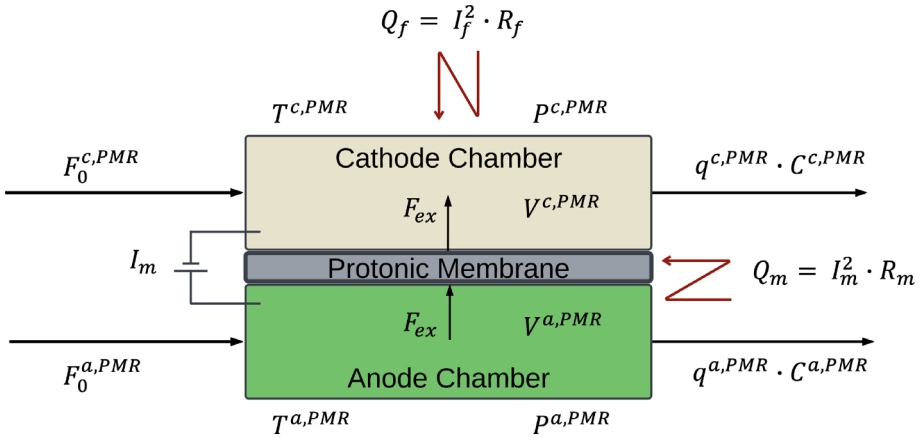

FIGURE 4 Control volume schematic for the anode and cathode chambers of the PMR unit. Key mass and energy inputs and outputs are labeled to match the reaction engineering models developed in Section 2.6 (Equations 11 to 15).

$$\dot{\boldsymbol{C}}^{c,PMR} = \frac{\boldsymbol{F}_0^{c,PMR} - q^{c,PMR}\boldsymbol{C}^{c,PMR} + \boldsymbol{F}_{ex}}{V^{c,PMR}} \tag{14a}$$

$$\boldsymbol{C}^{c,PMR} = \begin{bmatrix} C_{H_2O}^{c,PMR} \\ C_{H_2}^{c,PMR} \end{bmatrix}, \quad \boldsymbol{F}_0^{c,PMR} = \begin{bmatrix} F_{H_2O,0}^{c,PMR} \\ F_{H_2,0}^{c,PMR} \end{bmatrix}, \quad \boldsymbol{F}_{ex} = \begin{bmatrix} 0 \\ \frac{I_m}{2F} \end{bmatrix} \tag{14b}$$

with $\dot{C}_i^{c,PMR}$ defining the rate of change in the molar concentration of cathode species i contained in the vector $\boldsymbol{C}^{c,PMR}$. The ordinary differential equations equate the product of $\boldsymbol{C}^{c,PMR}$ with the scalar the cathode chamber volume $V^{c,PMR}$ to a balance of the cathodic feed flow rates contained in $\boldsymbol{F}_0^{c,PMR}$, the electrochemical molar generation rate of hydrogen that is modeled by $\boldsymbol{F}_{ex}$, and the outlet flow of each species in $\boldsymbol{q}^{c,PMR}\boldsymbol{C}^{c,PMR}$. The energy balance of the cathode chamber control volume accounts for the electric furnace heat and Joule-heating of the protonic membrane, the heat capacities of all reacting or inert species, heat generation from the compression of hydrogen to the elevated cathodic pressure, and heat losses to the external environment. Here, the energy balance for the cathode chamber is expressed as:

$$\dot{T}^{c,PMR} = \frac{f_h^{c,PMR} I_f^2 R_f + \sum F_{i,0}^{c,PMR} \int_{T_0^{c,PMR}}^{T^{c,PMR}} C_{p,i}\, dT' + \frac{I_m}{2F} \int_{T^{a,PMR}}^{T^{c,PMR}} C_{p,H_2}\, dT'}{\sum \rho_i^{c,PMR} C_{p,i} V^{c,PMR}} + \frac{U_h^{c,PMR} A_h^{c,PMR} (T^a - T^{c,PMR}) + \frac{1}{2} I_m^2 R_m + \frac{I_m}{4F} R T^{c,PMR} \ln\left(\frac{P^{c,PMR}}{P^{a,PMR}}\right)}{\sum \rho_i^{c,PMR} C_{p,i} V^{c,PMR}} \tag{15}$$

and the temperature rate of change, denoted as $\dot{T}^{c,PMR}$, is comprised of the fraction of source heat from the electrified furnace that is transferred to the cathode $f_h^{c,PMR}$ heat capacities of all cathodic species, the product of the cathodic overall heat transfer coefficient and cathodic heat transfer area ($U_h^{c,PMR} A_h^{c,PMR}$), Joule-heat generation, and heat of compression. Each gas species density is represented by ρ_i. Together, the mass and energy balance of the cathode chamber control volume, coupled with the ideal gas law, specify the total volumetric flow rate of the cathodic product stream in the following relation:

$$q^{c,PMR} = \left(\sum F_{l,0}^{c,PMR} + \frac{I_m}{2F}\right) \frac{R T^{c,PMR}}{P^{c,PMR}} + \frac{V^{c,PMR}}{T^{c,PMR}} \dot{T}^{c,PMR} \tag{16}$$

Thus, the analytic models developed in this section describe the full state of the PMR unit, defined as:

$$\boldsymbol{x}^{PMR} = \begin{bmatrix} \boldsymbol{C}^{a,PMR} \\ T^{a,PMR} \\ \boldsymbol{C}^{c,PMR} \\ T^{c,PMR} \end{bmatrix} \tag{17}$$

and $\boldsymbol{x}^{PMR}$ is a state vector that can be transferred from the state estimator to the optimizer of a model predictive controller.

For a kinetically-dominated operating regime, we consider the nominal steady state of all control scenarios to have a feed methane flow rate of 16.2 sccm, no applied electric current, and an initial anodic bubbler temperature of 120°C. The ratio of the characteristic methane diffusion time to the characteristic reaction time of the PMR is on the order of 10^{-1} for a methane feed flow rate of 16.2 sccm and reformer temperature of 732°C. The expected range of regulation for these process parameters during control is 16.0 to 30.0 sccm, 0.00 to 10.0 A, and 120 to 126°C, respectively. Key process disturbances, all stochastic in nature, are related to changes in the PMR current-voltage response, catalyst deactivation due to carbon formation side-reactions, and pressure oscillations throughout the bubbler and reformer chambers.

3 | CONTROL PROBLEM FORMULATION AND CONTROLLER DESIGN

3.1 | Classification of manipulated and controlled variables

Economically, the most important target variables for the PMR system are the purified y_1 and overall y_2 hydrogen production rates. In terms of anode conductivity, methane conversion, reaction rates, and catalyst activity,[14] a sufficient steam-to-carbon ratio y_3 in the initial reactant mixture is essential. The developed control architecture must regulate all three of these variables. There exist four control degrees of freedom to regulate the inlet and outlet states of the PMR unit and two control degrees of freedom to regulate the inlet and outlet states of the anodic bubbler. Preliminary experiments provide a physical intuition as to the manipulated variables directly impacting the proposed controlled variables, these input-output pairings of manipulated and controlled variables are: the electrical current u_1 for direct control of the hydrogen purification rate, the methane feed flow rate u_2 to regulate the anodic hydrogen production rate, and the temperature setpoint of a field PD-controller u_3 to maintain the anodic steam-to-carbon ratio of reactants. To confirm the controllability of all variable couplings, a steady-state relative gain array (RGA) was developed from the dynamic reactor engineering models in Section 2.6 as follows:

$$\boldsymbol{RGA}_{init} = \begin{bmatrix} 1.00 & 0 & 0 \\ 0 & 1.17 & -0.17 \\ 0 & -0.17 & 1.17 \end{bmatrix} \tag{18}$$

$$\boldsymbol{RGA}_{max} = \begin{bmatrix} 1.00 & 0 & 0 \\ 0 & 0.74 & 0.26 \\ 0 & 0.26 & 0.74 \end{bmatrix} \tag{19}$$

Equations (18) and (19) are the steady-state gain array calculations for the u_1, u_2, and u_3 control inputs, and y_1, y_2, and y_3 controlled outputs at the initial and maximum PMR operating conditions. The gain array for the initial set of operating conditions at the nominal steady-state is $\boldsymbol{RGA}_{init}$. At the upper bound of the PMR system operating domain, $\boldsymbol{RGA}_{max}$ is calculated for 10.0 A, 35.0 sccm, and 125°C. For both sets

of operating conditions, mild interactions are expected for u_2, u_3, y_2, and y_3. Physically, this multivariable coupling can be explained by the inextricable dependence of the hydrogen production rate on the steam-to-carbon ratio.

In the real PMR process, the only way to electrochemically separate hydrogen through a protonic membrane is by supplying an electric current, thus explaining the λ_{11} of the RGA matrices being equal to 1.00 for every set of operational conditions. However, the proposed process models do not contain mathematical terms for membrane conductivity, which is a function of the reformer temperature and the partial pressures of steam on the reformer electrode surfaces. For this reason, the true independence and stability of the control input-output pairings were experimentally tested in Peters et al.[18] to demonstrate the safe operation of the reforming system and the multi-input multi-output controller effectiveness on the PMR process.

3.2 | Control objectives and constraints

Unlike classical control formulations, the MPC framework enables control engineers to restrict changes in process parameters within desired domains, which actively constrains control actions. Thus, MPC designs for the protonic membrane reformer unit may incorporate constraints on the discrete derivatives of the applied electric current to the system. Such constraints protect the protonic membrane surface from rapid Joule-heating, hydrogen depletion, or local dehydration of the anode surface. The proposed control objectives, put forth as follows, incorporate constraints on the operational domain of the reforming system and the rates of the reformer temperature change to improve the electrochemical performance of the protonic membrane cell. The control objectives for the PMR process are:

1. All control actions, regardless of closed-loop effectiveness, will not induce runaway system temperatures or pressures. Hydrogen depletion or electrical damage to system components is likewise prohibited.
2. Control actions must be bound by upper and lower operational limits for the reformer temperature and pressure, the feed flow rate of methane, and the feed flow rate of steam.
3. An effective control design will reproducibly achieve all controlled variable target setpoints and do so in less time than comparable classical feedback loops.
4. The proposed constraints on the hydrogen purification rate control loop must limit changes in the reformer chamber to $\pm 5^{\circ}\text{C}\cdot\text{min}^{-1}$ to protect the surface morphology of the anode and catalytic activity.
5. Under irreversible disturbance conditions, the DMPC architecture will successfully adapt the state estimation vector to the modified steady-states of the PMR subprocesses to ensure optimizer convergence.
6. Failures in optimizer convergence during single or multiple sampling intervals must not produce dangerous or damaging control actions. Convergence failures should be limited to less than 5% of all sampling steps.
7. Control scenario S1 will set the automatic setpoint generator to 75% of the total hydrogen available in the system at t_{-900s}. Following the successful execution of control scenario S1, control scenario S2 will increase the recovery rate setpoint to 90% of the total hydrogen available in the system at t_{-900s}. Control scenario S2 aims to test the input constraints on u_1 that should allow for higher current densities and hydrogen extraction rates. A PMR control system that establishes these control objectives under experimental evaluation can be considered robust and adequate for advanced automation efforts.

3.3 | Disturbance observer and augmented model

Achieving the desired control objectives fundamentally depends on the accuracy of the model employed in MPC. Specifically, within a DMPC framework, subsystem models are utilized to predict outputs. Furthermore, due to sensor constraints, such as infrequent measurements, inherent delays, and difficulty measuring certain process variables, these models also function as estimators, providing frequent estimates of all state variables.[24] However, given the potential for, and observation of steady-state drifts in the hydrogen generation control loop, state estimation through the use of offline fittings of the physics-based models is not sufficient. The pure model in Section 2.6 does not account for catalyst aging in the real process, which leads to the observed plant-model mismatch. Therefore, the overall state vector must be augmented in real-time to account for any transient or permanent disturbance phenomena that cause steady-state deviations in $\hat{y}_j$ from y_j. To that end, a disturbance observer is developed in this section to compensate for plant-model mismatch throughout the control experiment. State estimation by way of an offset-free extended state observer allows for accurate state predictions when the control system is under the stress of stochastic and evolving disturbance phenomena. A state vector for the following general nonlinear system is formulated as follows:

$$\dot{\boldsymbol{x}} = \boldsymbol{F}(\boldsymbol{x}, \boldsymbol{u}) \tag{20a}$$

$$\boldsymbol{y} = \boldsymbol{h}(\boldsymbol{x}) \tag{20b}$$

with $\boldsymbol{x} \in \mathbb{R}^n$ denoting the predicted state vector from the PMR unit and anodic bubbler process models, and $\boldsymbol{u} \in \mathbb{R}^m$ representing the control input vector. $\boldsymbol{F} : \mathbb{R}^n \times \mathbb{R}^m \to \mathbb{R}^n$ is the model from the physical information discussed in Sections 2.5 and 2.6. The target variable prediction vector $\boldsymbol{y} \in \mathbb{R}^k$ is determined by transforming $\boldsymbol{x} \in \mathbb{R}^n$ by $\boldsymbol{h} : \mathbb{R}^n \to \mathbb{R}^k$ to obtain the predicted state of the controlled vector.

The following disturbance observer formulation, adopted from the general framework of Equation (20), is used to accumulate prediction errors over time with a disturbance state. This allows the dynamic model to compensate for prediction errors by introducing an additional disturbance state (extended state) $\boldsymbol{\xi} \in \mathbb{R}^n$ to the state estimation method. Building on this offset-free method, the unknown input observer (UIO), which is a type of disturbance observer, explicitly

estimates disturbances and integrates them into the system model.[25] In this technique, the disturbances are assumed to be generated by an exogenous system[26,27] in which the general state vector $\boldsymbol{F}:\mathbb{R}^n\times\mathbb{R}^m\rightarrow\mathbb{R}^n$ is modified by a disturbance observer term in the following relation[28–30]:

$$\dot{\hat{\boldsymbol{x}}}=\boldsymbol{F}(\hat{\boldsymbol{x}},\boldsymbol{u})+\boldsymbol{B}_d\boldsymbol{d} \tag{21a}$$

$$\hat{\boldsymbol{y}}=\boldsymbol{h}(\hat{\boldsymbol{x}},\boldsymbol{u}) \tag{21b}$$

$$\dot{\boldsymbol{\xi}}=\boldsymbol{W}\boldsymbol{\xi} \tag{21c}$$

$$\boldsymbol{d}=\boldsymbol{V}\boldsymbol{\xi} \tag{21d}$$

with $\hat{\boldsymbol{x}}\in\mathbb{R}^n$ representing the modified state vector that is governed by the predicted system dynamics and the accumulation of external disturbances. The auxiliary disturbance state $\boldsymbol{\xi}\in\mathbb{R}^n$ corrects for inaccuracies in the pure model due to plant-model mismatch by accumulating the disturbance-induced model error over time, and the disturbance matrix is designated as $\boldsymbol{B}_d\in\mathbb{R}^{n\times n}$. The additional disturbance state $\boldsymbol{\xi}\in\mathbb{R}^n$ corrects for inaccuracies in the pure model by accumulating the disturbance-induced model error over time. $\boldsymbol{B}_d\in\mathbb{R}^{n\times n}$ represents the disturbance matrix, and $\tilde{\boldsymbol{d}}\in\mathbb{R}^n$ estimates the disturbance $\boldsymbol{d}\in\mathbb{R}^n$ in Equation (21) calculated using $\boldsymbol{V}\tilde{\boldsymbol{\xi}}\in\mathbb{R}^n$.

For state estimation, a disturbance observer is further integrated into the extended state observer:

$$\dot{\tilde{\boldsymbol{x}}}=\boldsymbol{F}(\tilde{\boldsymbol{x}},\boldsymbol{u})+\boldsymbol{L}_x(\boldsymbol{y}_r-\tilde{\boldsymbol{y}})+\boldsymbol{B}_d\tilde{\boldsymbol{d}} \tag{22a}$$

$$\tilde{\boldsymbol{y}}=\boldsymbol{h}(\tilde{\boldsymbol{x}}) \tag{22b}$$

$$\dot{\tilde{\boldsymbol{\xi}}}=\boldsymbol{W}\tilde{\boldsymbol{\xi}}+\boldsymbol{L}_{\xi}(\boldsymbol{y}_r-\tilde{\boldsymbol{y}}) \tag{22c}$$

$$\tilde{\boldsymbol{d}}=\boldsymbol{V}\tilde{\boldsymbol{\xi}} \tag{22d}$$

where $\tilde{\boldsymbol{x}}\in\mathbb{R}^n$ is the modified state vector governed by the predicted system dynamics with the augmented state estimator and the accumulation of external disturbances. $\boldsymbol{L}_x\in\mathbb{R}^{n\times k}$ and $\boldsymbol{L}_{\xi}\in\mathbb{R}^{n\times k}$ serve as the observer gains, and $(\boldsymbol{y}_r-\tilde{\boldsymbol{y}})\in\mathbb{R}^k$ is the error between the real target output $\boldsymbol{y}_r\in\mathbb{R}^k$ and the expected target output $\tilde{\boldsymbol{y}}\in\mathbb{R}^k$.

In process control literature, many observer-augmented models have proven to be stable and offset-free by incorporating the error dynamics of systems.[31,32] However, most observers consider discrete-time systems. In this paper, the stability and asymptotic error of the state observer are considered for a real, continuous-time, and nonlinear process with uncertain disturbances, which are represented by the following equations:

$$\dot{\boldsymbol{x}}_r=\boldsymbol{F}_r(\boldsymbol{x}_r,\boldsymbol{u},\boldsymbol{w}_r) \tag{23a}$$

$$\boldsymbol{y}_r=\boldsymbol{h}(\boldsymbol{x}_r) \tag{23b}$$

where $\boldsymbol{x}_r\in\mathbb{R}^n$ and $\boldsymbol{y}_r\in\mathbb{R}^k$ are the real process state vector and the real output vector, respectively. $\boldsymbol{F}_r:\mathbb{R}^n\times\mathbb{R}^n\times\mathbb{R}^{n_w}\rightarrow\mathbb{R}^n$ represents the function that captures the dynamic behavior of the experimental process. $\boldsymbol{w}=\boldsymbol{w}(t)\in\mathbb{R}^{n_w}$ is assumed to be the mismatch between the real process and the model, uncertainty, or unknown external disturbances, defined as follows:

$$\boldsymbol{w}:=\boldsymbol{F}_r(\boldsymbol{x}_r,\boldsymbol{u},\boldsymbol{w}_r)-\boldsymbol{F}(\boldsymbol{x}_r,\boldsymbol{u}) \tag{24}$$

This difference is also asymptotically constant,[31] and the following limits hold true:

$$\lim_{t\rightarrow\infty}\boldsymbol{w}(t)=\overline{\boldsymbol{w}},\quad\lim_{t\rightarrow\infty}\dot{\boldsymbol{w}}(t)=\boldsymbol{0} \tag{25}$$

To be consistent with the format of the observer-based model, we define $\boldsymbol{d}_r=\frac{\boldsymbol{w}}{\boldsymbol{B}_d}$, $\boldsymbol{\xi}_r=\frac{\boldsymbol{d}_r}{\boldsymbol{V}}$, and $\dot{\boldsymbol{\xi}}_r=\frac{\partial\boldsymbol{\xi}_r}{\partial\boldsymbol{d}_r}\frac{\partial\boldsymbol{d}_r}{\partial\boldsymbol{w}}\dot{\boldsymbol{w}}=\frac{\dot{\boldsymbol{w}}}{\boldsymbol{V}\boldsymbol{B}_d}$. Hence, the real process can be represented by the following equations:

$$\dot{\boldsymbol{x}}_r=\boldsymbol{F}(\boldsymbol{x}_r,\boldsymbol{u})+\boldsymbol{w}=\boldsymbol{F}(\boldsymbol{x}_r,\boldsymbol{u})+\boldsymbol{B}_d\boldsymbol{d}_r \tag{26a}$$

$$\boldsymbol{y}_r=\boldsymbol{h}(\boldsymbol{x}_r) \tag{26b}$$

$$\dot{\boldsymbol{\xi}}_r=\frac{\dot{\boldsymbol{w}}}{\boldsymbol{V}\boldsymbol{B}_d} \tag{26c}$$

$$\boldsymbol{d}_r=\boldsymbol{V}\boldsymbol{\xi}_r \tag{26d}$$

The dynamics of the errors between the estimation states and real states ($\boldsymbol{e}_x=\boldsymbol{x}_r-\tilde{\boldsymbol{x}}\in\mathbb{R}^n$) along with the disturbance error dynamics ($\boldsymbol{e}_d=\boldsymbol{d}_r-\tilde{\boldsymbol{d}}\in\mathbb{R}^n$) are calculated as follows:

$$\dot{\boldsymbol{e}}_x=\dot{\boldsymbol{x}}_r-\dot{\tilde{\boldsymbol{x}}}=\boldsymbol{F}(\boldsymbol{x}_r,\boldsymbol{u})-\boldsymbol{F}(\tilde{\boldsymbol{x}},\boldsymbol{u})-\boldsymbol{L}_x\left[\boldsymbol{h}(\boldsymbol{x}_r)-\boldsymbol{h}(\tilde{\boldsymbol{x}})\right]+\boldsymbol{B}_d\,\boldsymbol{e}_d \tag{27a}$$

$$\dot{\boldsymbol{e}}_d=\dot{\boldsymbol{d}}_r-\dot{\tilde{\boldsymbol{d}}}=\boldsymbol{V}\left[\frac{\dot{\boldsymbol{w}}}{\boldsymbol{V}\boldsymbol{B}_d}-\boldsymbol{W}\tilde{\boldsymbol{\xi}}+\boldsymbol{L}_{\xi}(\boldsymbol{h}(\tilde{\boldsymbol{x}})-\boldsymbol{h}(\boldsymbol{x}_r))\right] \tag{27b}$$

At steady state ($t\rightarrow\infty$), the system is linearized around the equilibrium state $\boldsymbol{x}^*\in\mathbb{R}^n$. Combining with Equation (25) and designing $\boldsymbol{W}=\boldsymbol{0}$, we can obtain the following linearized error dynamics:

$$\begin{bmatrix}\dot{\boldsymbol{e}}_x\\ \dot{\boldsymbol{e}}_d\end{bmatrix}=\begin{bmatrix}\boldsymbol{A}^*-\boldsymbol{L}_x\boldsymbol{C}^* & \boldsymbol{B}_d\\ -\boldsymbol{V}\boldsymbol{L}_d\boldsymbol{C}^* & \boldsymbol{0}\end{bmatrix}\begin{bmatrix}\boldsymbol{e}_x\\ \boldsymbol{e}_d\end{bmatrix}=\mathcal{M}\begin{bmatrix}\boldsymbol{e}_x\\ \boldsymbol{e}_d\end{bmatrix} \tag{28}$$

with the Jacobian matrices defined as $\boldsymbol{A}^*:=\frac{\partial\boldsymbol{F}}{\partial\boldsymbol{x}}\big|_{(\boldsymbol{x}^*,\boldsymbol{u})}$ and $\boldsymbol{C}^*:=\frac{\partial\boldsymbol{h}}{\partial\boldsymbol{x}}\big|_{\boldsymbol{x}^*}$. $\boldsymbol{L}_x$, $\boldsymbol{L}_d$, $\boldsymbol{V}$, and $\boldsymbol{B}_d$ should also be designed to ensure $\mathcal{M}$ is a Hurwitz matrix to guarantee that the estimation of errors converge to zero. Asymptotically, at $t\rightarrow\infty$ from Equation (28), the following relationship is obtained:

$$(\boldsymbol{A}^*-\boldsymbol{L}_x\boldsymbol{C}^*)\boldsymbol{e}_x=\boldsymbol{0} \tag{29a}$$

$$-\boldsymbol{V}\boldsymbol{L}_d\boldsymbol{C}^*\boldsymbol{e}_d=\boldsymbol{0} \tag{29b}$$

Therefore, the augmented model can achieve exact state tracking and disturbance compensation at steady state:

$$\lim_{t\to\infty}\tilde{\boldsymbol{x}}-\boldsymbol{x}_r=\boldsymbol{0},\quad \lim_{t\to\infty}\tilde{\boldsymbol{d}}=\boldsymbol{B}_d^{-1}\overline{\boldsymbol{w}} \tag{30}$$

which indicates that the $\tilde{\boldsymbol{d}}\in\mathbb{R}^n$ term in Equation (21a) can compensate for the plant-model mismatch caused by $\boldsymbol{w}$ at the final steady state, which demonstrates Equation (22) can be utilized as the state vector and error evolution estimator.

In the context of MPC, this estimated state vector serves as the initial condition of the optimizer state predictions, and the estimated error is augmented following Equation (21) as follows:

$$\dot{\overline{\boldsymbol{x}}}=\overline{\boldsymbol{F}}(\overline{\boldsymbol{x}},\boldsymbol{u}) \tag{31a}$$

$$\overline{\boldsymbol{y}}=\boldsymbol{h}(\overline{\boldsymbol{x}}) \tag{31b}$$

$$\overline{\boldsymbol{x}}=\begin{bmatrix}\tilde{\boldsymbol{x}}\\ \tilde{\boldsymbol{\xi}}\end{bmatrix},\quad \overline{\boldsymbol{F}}(\overline{\boldsymbol{x}},\boldsymbol{u})=\begin{bmatrix}\hat{\boldsymbol{F}}(\tilde{\boldsymbol{x}},\boldsymbol{u})+\boldsymbol{B}_d\tilde{\boldsymbol{d}}\\ \boldsymbol{W}\tilde{\boldsymbol{\xi}}\end{bmatrix} \tag{31c}$$

For subsystem j, this augmented model takes the form:

$$\dot{\overline{\boldsymbol{x}}}_j=\overline{\boldsymbol{F}}_j(\overline{\boldsymbol{x}}_j,\boldsymbol{u}_j) \tag{32a}$$

$$\overline{\boldsymbol{y}}_j=\boldsymbol{h}_j(\overline{\boldsymbol{x}}_j) \tag{32b}$$

$$\overline{\boldsymbol{x}}_j=\begin{bmatrix}\tilde{\boldsymbol{x}}_j\\ \tilde{\boldsymbol{\xi}}_j\end{bmatrix},\quad \overline{\boldsymbol{F}}_j(\overline{\boldsymbol{x}}_j,\boldsymbol{u}_j)=\begin{bmatrix}\hat{\boldsymbol{F}}_j(\tilde{\boldsymbol{x}}_j,\boldsymbol{u}_j)+\boldsymbol{B}_{dj}\tilde{\boldsymbol{d}}_j\\ \boldsymbol{W}_j\tilde{\boldsymbol{\xi}}_j\end{bmatrix} \tag{32c}$$

This augmented model is comprised not only of the intrinsic behavior of physical properties but also of the mismatch compensation of experimental data deviations, thereby motivating the development of a generalized hybrid physics-data-driven model.

3.4 | Hybrid physics-data-driven model development

In Section 3.3, a hybrid physics-data-driven model was developed. By embedding deterministic physical equations (e.g., mass, energy, and charge balances), a base model can be generated to capture the chemical physics of the PMR process. Simultaneously, an augmented data-driven correction term captures unmodeled effects, such as unknown disturbances and parameter changes. Specifically, the data-driven correction can be further divided into two processes: Offline data-driven correction and online data-driven correction. This is one of many ways to build a model around operational uncertainty, with other suitable methods including Bayesian reinforcement learning schemes or Gaussian processes for uncertainty quantification.[33]

In general, this physics-data-driven model can be expressed as follows[34]:

$$\dot{\boldsymbol{x}}_{pd}=\boldsymbol{F}(\boldsymbol{x}_{pd},\boldsymbol{u})+\boldsymbol{F}_d(\boldsymbol{x}_{pd},\boldsymbol{u}) \tag{33}$$

where $\boldsymbol{x}_{pd}\in\mathbb{R}^n$ is the state vector of physics-data-driven model. $\boldsymbol{F}:\mathbb{R}^n\times\mathbb{R}^m\to\mathbb{R}^n$ is the physics-based function. $\boldsymbol{F}_d:\mathbb{R}^n\times\mathbb{R}^m\to\mathbb{R}^n$ is the data-based function. Considering the system described by Equations (23) and (24), the following relationship is also obtained at steady state:

$$\boldsymbol{F}_d(\boldsymbol{x}_{pd},\boldsymbol{u})=\boldsymbol{w}. \tag{34}$$

This mismatch (or bias, $\boldsymbol{w}$) is typically compensated via machine learning models in control engineering literature.[34–36] However, such models take considerable computational effort and require large datasets. In this work, a disturbance observer is added to the physics-based model to enhance the process model accuracy. The compensation term ($\tilde{\boldsymbol{d}}$ or $\tilde{\boldsymbol{\xi}}$) is initially designed to fit offline data and is adaptively changed to correct experimental errors in an online manner throughout the control time.

3.5 | Decentralized model predictive control structure

A decentralized MPC architecture is proposed that regulates the steam-to-carbon ratio of reactants, along with the hydrogen generation and purification subprocesses. The loss function defined in Equation (35d) penalizes process-setpoint deviations and advances control actions to minimize setpoint deviations and bring the process to its target state. The DMPC architecture employs the models in Sections 2.5 and 2.6, augmented with the disturbance observer discussed in Section 3.3, to survey the future states of the PMR over a prediction horizon based on immediate and future control actions. The discretized feedback information from the process sensors in Figure 5 allows an online accounting of disturbance effects on model errors, which provides a mathematical impetus for model correction via the disturbance estimator (Equation 22d) to achieve zero steady-state offset.

The theoretical implementation of a DMPC architecture in Cui et al.[14] demonstrates the stability and computational efficiency of the proposed control design in an ideal PMR system with arbitrary and ordered disturbance phenomena. Likewise, in Peters et al.,[18] a classical multi-input multi-output control architecture based on identical input-out pairings showed reproducible setpoint achievement during multi-setpoint tracking control scenarios. Here, the subsystem objective functions are defined for three closed-loop model predictive controllers. Specifically, the objective functions minimize setpoint deviations of the estimated states of the PMR system. The control effort to reach each target state is also minimized by the DMPC objective functions. The control input bounds and input constraints on applied electric current, the feed methane flow rate, and PD-

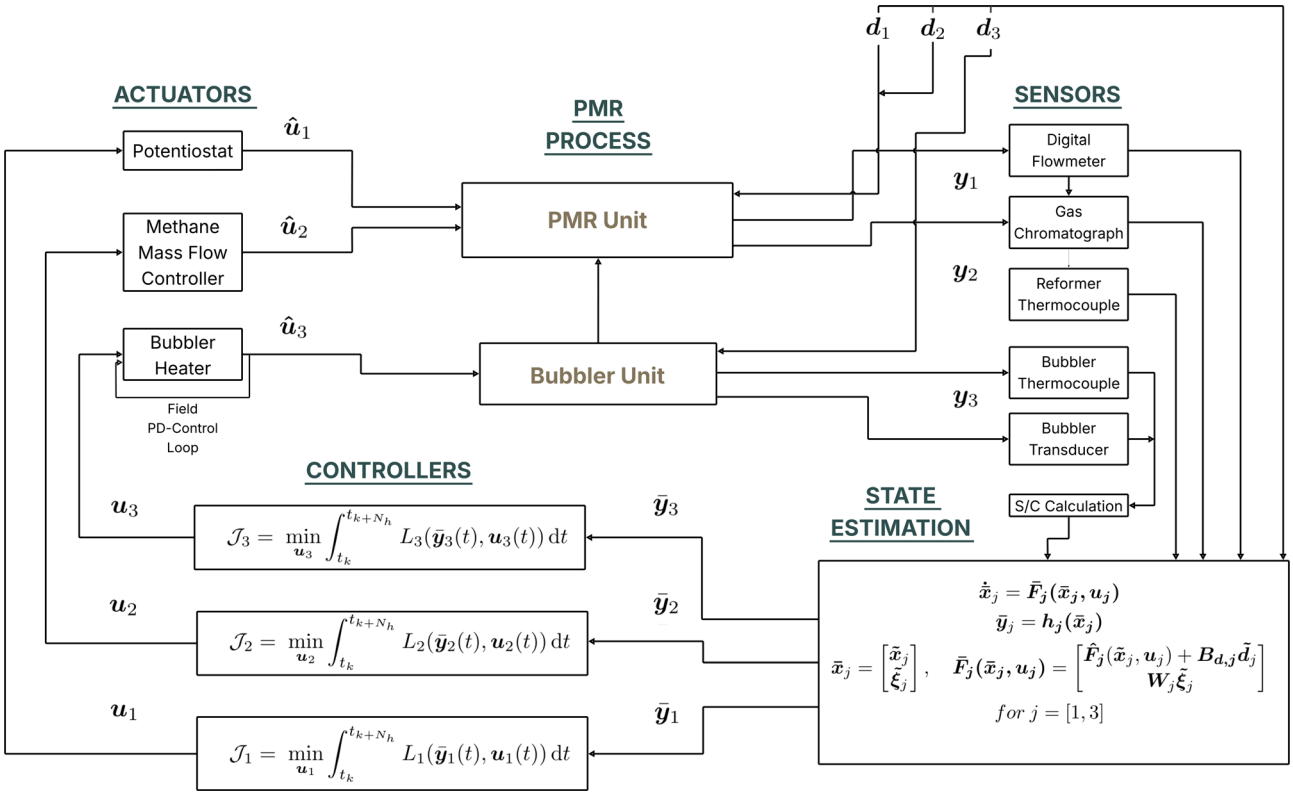

FIGURE 5 Representation of the closed-loop DMPC architecture for regulating the steam-to-carbon ratio, hydrogen generation, and hydrogen purification rates in the experimental PMR system.

controller temperature setpoint are also assigned to each controller. To initialize each DMPC subsystem for each sampling time, the state estimator developed in Section 3.3 provides the estimated state vector at t_k. Likewise, the model accuracy from augmentation of the process models via the disturbance observer terms improves the likelihood of solution convergence, despite stochastic experimental disturbance phenomena. The general formulation of the subsystem minimization problems for the three MPC regulators is expressed as:

$$\mathcal{J}_j = \min_{\boldsymbol{u}_j} \int_{t_k}^{t_{k+N_h}} L_j(\overline{\boldsymbol{y}}_j(t), \boldsymbol{u}_j(t))\,dt \tag{35a}$$

$$\text{s.t. } \dot{\overline{\boldsymbol{x}}}_j(t) = \overline{\boldsymbol{F}}_j(\overline{\boldsymbol{x}}_j(t), \boldsymbol{u}_j(t)), \quad \overline{\boldsymbol{x}}_j(t_k) = \boldsymbol{x}_j(t_k) \tag{35b}$$

$$\overline{\boldsymbol{y}}_j(t) = \boldsymbol{h}_j(\overline{\boldsymbol{x}}_j(t)) \tag{35c}$$

$$\begin{aligned} L_j(\overline{\boldsymbol{y}}_j(t), \boldsymbol{u}_j(t)) = &(\overline{\boldsymbol{y}}_j(t) - \boldsymbol{y}_{j,sp}(t))^{\top} \boldsymbol{A}_j (\overline{\boldsymbol{y}}_j(t) - \boldsymbol{y}_{j,sp}(t)) \\ &+ (\boldsymbol{u}_j(t) - \boldsymbol{u}_{j,sp}(t))^{\top} \boldsymbol{B}_j (\boldsymbol{u}_j(t) - \boldsymbol{u}_{j,sp}(t)) \end{aligned} \tag{35d}$$

$$t \in [t_k, t_{k+N_h}) \tag{35e}$$

$$\|\boldsymbol{u}_j(t_k) - \boldsymbol{u}_j(t_{k-1})\| \le \Delta \boldsymbol{u}_{\text{limit},j} \tag{35f}$$

$$\boldsymbol{u}_j(t) \in U_j \quad \forall t \in [t_k, t_{k+N_h}) \tag{35g}$$

where $\boldsymbol{x}_j(t_k) \in \mathbb{R}^n$ represents the initial state vector for subsystem j at $t = t_k$ estimated by Equation (22). Equations (35b) and (35c) are the same as Equation (32). Through these equations, the state vector $\overline{\boldsymbol{x}}_j(t)$ and the output vector $\overline{\boldsymbol{y}}_j(t)$ for subsystem j over the defined horizon time (t_k to t_{k+N_h}) is estimated. This estimated output vector is involved in Equation (35d) to evaluate the distance between it and setpoints. The optimization problem minimizes this distance (Equation 35a). $\boldsymbol{A}_j$ and $\boldsymbol{B}_j$ are weighted parameters for the output vector and the control action vector, respectively. Furthermore, the optimization problem is constrained by the control input change rate (Equation 35f) and control input magnitude (Equation 35g). These constraints are applied to satisfy the control objectives discussed in Section 3.2. Specifically, for DMPC 1, or subsystem 1, the input is bound to the set $U_1 = \{u_1 \mid 0.00\,A \le u_1 \le 12.1\,A\}$ and the rate of change in the the input is constrained to $\|u_1(t_k) - u_1(t_{k-1})\| \le 0.10\,A$. DMPC 2, is also constrained, bound to the set $U_2 = \{u_2 \mid 10.0\,sccm \le u_2 \le 40.0\,sccm\}$ and limited to $\|u_2(t_k) - u_2(t_{k-1})\| \le 0.02\,sccm$. Finally, the range and input rate of change limit for DMPC 3 is defined by $U_3 = \{u_3 \mid 110^{\circ}C \le u_3 \le 130^{\circ}C\}$ and $\|u_3(t_k) - u_3(t_{k-1})\| \le 0.01^{\circ}C$. The overall decentralized control architecture, including controllers, actuators, sensors, and process integration, is provided in Figure 5.

For adaptive setpoint decisions in the DMPC 1 closed-loop structure, $y_{sp,1}$ is determined by the manual setpoint or automated setpoint generator. The objective of the setpoint generator, defined as Algorithm 1, is to calculate the separation rate of hydrogen based on the

Algorithm 1 **Automatic Setpoint Calculation for Controller 1**

Input: Automatic Setpoint Enabled flag
if *Automatic Setpoint is Enabled* **then**
  Calculate total hydrogen inventory;
  Retrieve Anode H_2 and Cathode H_2 at time t_{-900s};
  Retrieve Inlet CH_4 and Inlet H_2 at current time t;
  Compute inventory-based $H_2 \leftarrow$ Anode H_2 + Cathode H_2;
  Compute inlet-based $H_2 \leftarrow 3.3 \times$ Inlet CH_4 + Inlet H_2;
  $H_2^{target} \leftarrow 0.75 \times \min(\text{inventory, inlet})$;
  Setpoint for Controller 1 $\leftarrow H_2^{target}$;
else
  Use manual setpoint entry for Controller 1;

availability of hydrogen in the system. This way, the DMPC 1 purification rate never exceeds the amount of hydrogen available in the anode chamber, preventing complete hydrogen depletion at the anode surface. The pseudocode is presented in Algorithm 1 below, where the notation t_{-900s} is used to denote that the calculation of the total available hydrogen is a value from 15 min prior to the calculation and change of the setpoint.

4 | OPEN-LOOP EXPERIMENTATION AND MODEL VALIDATION

The physics-data-driven models developed for the PMR system in Section 3.4 are now fit to the offline experimental input-output data via adjustable parameters for improved state estimation. With experimentally-validated predictions that determine the entire thermodynamic state of the PMR system via the lumped-parameter reformer, anodic bubbler, and hydrogen separation models, the state estimator will closely describe the dynamic evolution of the PMR system throughout the control time. The first step in connecting theoretical models to the actual thermodynamics of the PMR process is to perform step-change experiments for the manipulated variables and record the response of the target variables. Step-change experiments allow control engineers to survey the transient response times of the final control elements and controlled variables. Thus, open-loop step change experiments were used to examine the transient response times of the process. Preliminary experiments elucidate the dynamic characteristics of the actuators and process variables in the PMR system (Sections 2.5 and 2.6) for accurate forecasting of the system states.

4.1 | PMR system transient response

Documentation of system dynamics, subject to simultaneous changes in multiple process variables, establishes the intrinsic coordination between input and output variables, while also categorizing input-output variable pairings as aggressive, balanced, or ineffective. Specifically, scanning or ramping the manipulated input variables of the control scheme (Section 3.5) confirms the proposed physics of the process units and informs the tunings of the dynamic models, the state observer, and predictive controllers. To induce and record the transient response of the target variables in the PMR system, an electric current sweep rate of $8.00 \times 10-^{3}$ A·(5 s)$^{-1}$ was initiated at the 20th min of the transient experiment presented in Figure 6. The feed flow rate of methane and the bubbler temperature were also modulated at the 84th min and 92nd min, respectively.

The response of the PMR system to the continuous step-change schedule was on the order of seconds for the electric current and hydrogen purification variable coupling, whereas the methane feed and hydrogen generation variable coupling had a response time on the order of minutes. The settling time for the bubbler after modulating T_{sp} was also on the order of minutes. The discontinuation of all three manipulated variable ramps demonstrates that the system can achieve a new steady-state in a reasonable time scale for process control. However, the facile response of hydrogen separation and purification in response to changes in the applied electric current requires explicit constraints on u_1 due to the immediate impact on the reformer temperature that is observed in Figure 6. In fact, 9.00 A of electric current increased the reformer temperature by 90.0°C, and the initial step change from 0.00 to 1.90 A increased the reformer temperature at a rate of 10.0°C·min^{-1}. The ramp change in the manipulated variables also induced positive effects on the process, such as a full equilibrium shift toward the complete conversion of methane and a selectivity shift from CO to CO_2. Additionally, increases in the SMR and WGS reaction kinetics increased the conversion rate of methane, even as more methane was fed to the system (Figure 6B), indicating negligible mass transfer limitations. To determine the dynamic characteristics of the PMR system for predictive control, the estimation method presented in Section 3.3, comprised of

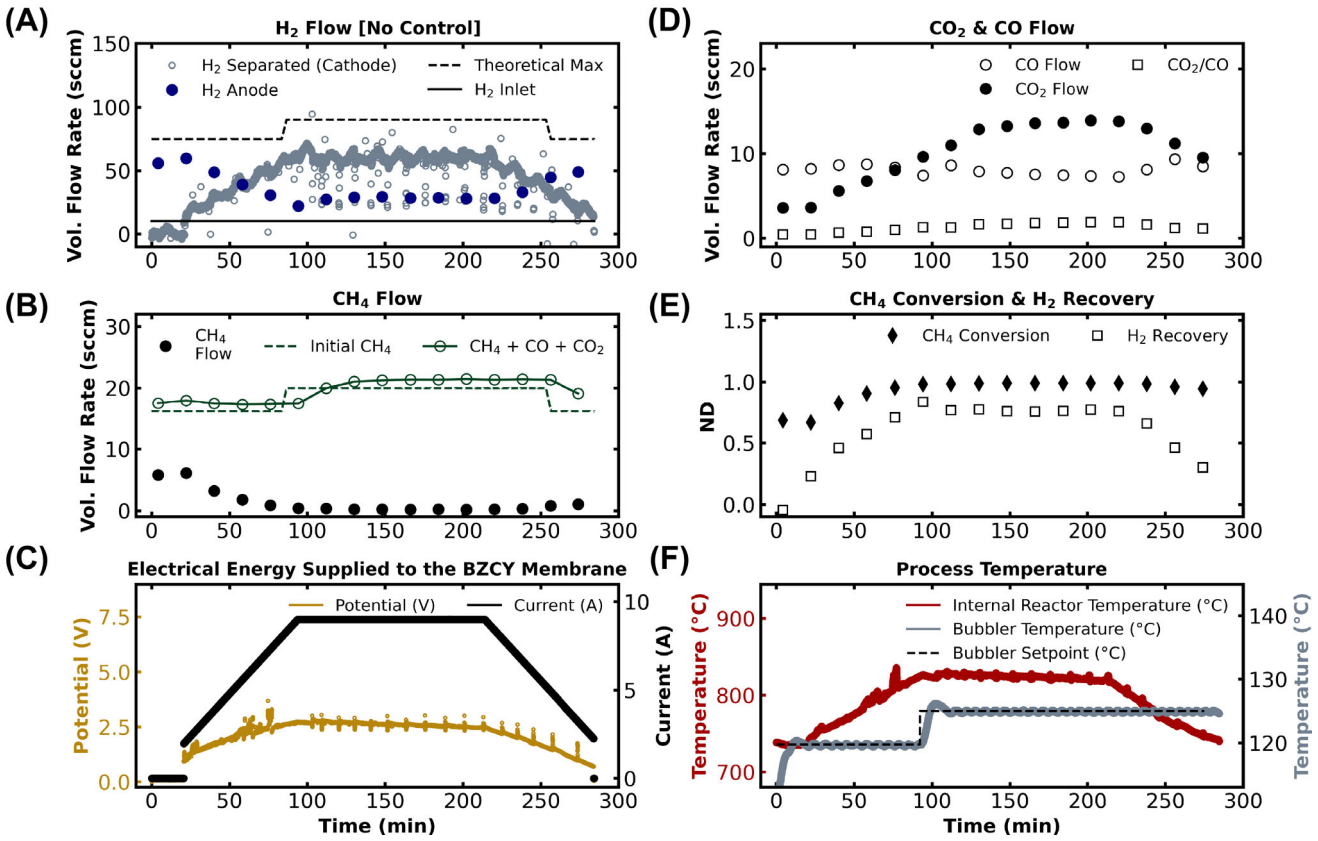

FIGURE 6 Transient experimental results induced by an electric current sweep rate of 8.00×10^{-3} A·(5 s)$^{-1}$. (A) Anodic hydrogen generation rates and the hydrogen separation rate into the cathode, (B) Carbon species balance and methane flow rates, (C) Applied current and measured potential in the MEA, (D) Carbon oxide generation rates and selectivity, (E) Hydrocarbon conversion and hydrogen recovery rates, and (F) Anodic bubbler and internal PMR unit temperatures.

physics-data-driven-based models for the anodic bubbler and PMR units, was tested on an additional set of dynamic input data (Section 4.2).

4.2 | Experimental data-fitting via model parameter adaptation

In Cui et al.,[14] only steady-state and dynamic kinetic modeling (Equation 3) were experimentally validated with Xu and Froment[22] plug flow kinetic parameters. In Figure 7, the hydrogen purification rate, hydrogen generation rate kinetics, and anodic bubbler are all evaluated with dynamic and steady-state experimental data. A new data-fitting exercise was conducted in this study, given the reactivity of the system changes over time; thus, the experimentally-adjusted parameters of the state estimation models need to fit the system in its most recent operational condition. Figure 7A provides a cyclic voltammetry plot of the protonic membrane cell at a 10^{-1} A·min^{-1} electric current sweep rate. Based on the PMR electron balance (Equation 6), assuming 100% faradaic efficiency for current densities up to 0.55 A·cm^{-2}, $\frac{I_m}{2F}$ captures the average separation rate of hydrogen through the protonic membrane with a mean absolute model error of 3.48 sccm. Not only does the 100% faradaic efficiency assumption hold, but the excellent agreement between the model and experimental hydrogen separation rate means that the predictions for the most important target variable in the process are reproducibly accurate.

The steady-state experiments in Figure 7B match the lumped-parameter anodic reaction model in Figure 13 when W_{cat} values in the ***R*** vector of Equation (11) are all equal to 13.0 mg. The mean absolute prediction error at this active catalyst weight for all species was 0.95 sccm, and the average standard deviation for all steady state experimental measurements was ±0.73 sccm. For anodic hydrogen specifically, the most important prediction for the second-loop controller, a mean absolute model error for anodic hydrogen of 0.10 sccm was observed. Thus, the lumped-parameter reaction engineering model accurately captures the state change in the anodic product stream as the steady-state reformer temperature is modulated. Attention must also be given to the steady-state anodic hydrogen predictions within the temperature window of 730 to 810°C so that the temperature range within which the control experiment is conducted is properly modeled. At the elevated reformer temperatures, there is increasing variability in the experimental data, and a larger error is observed between the data and the lumped-parameter model for anodic hydrogen predictions, further justifying the need for state estimation with error compensation.

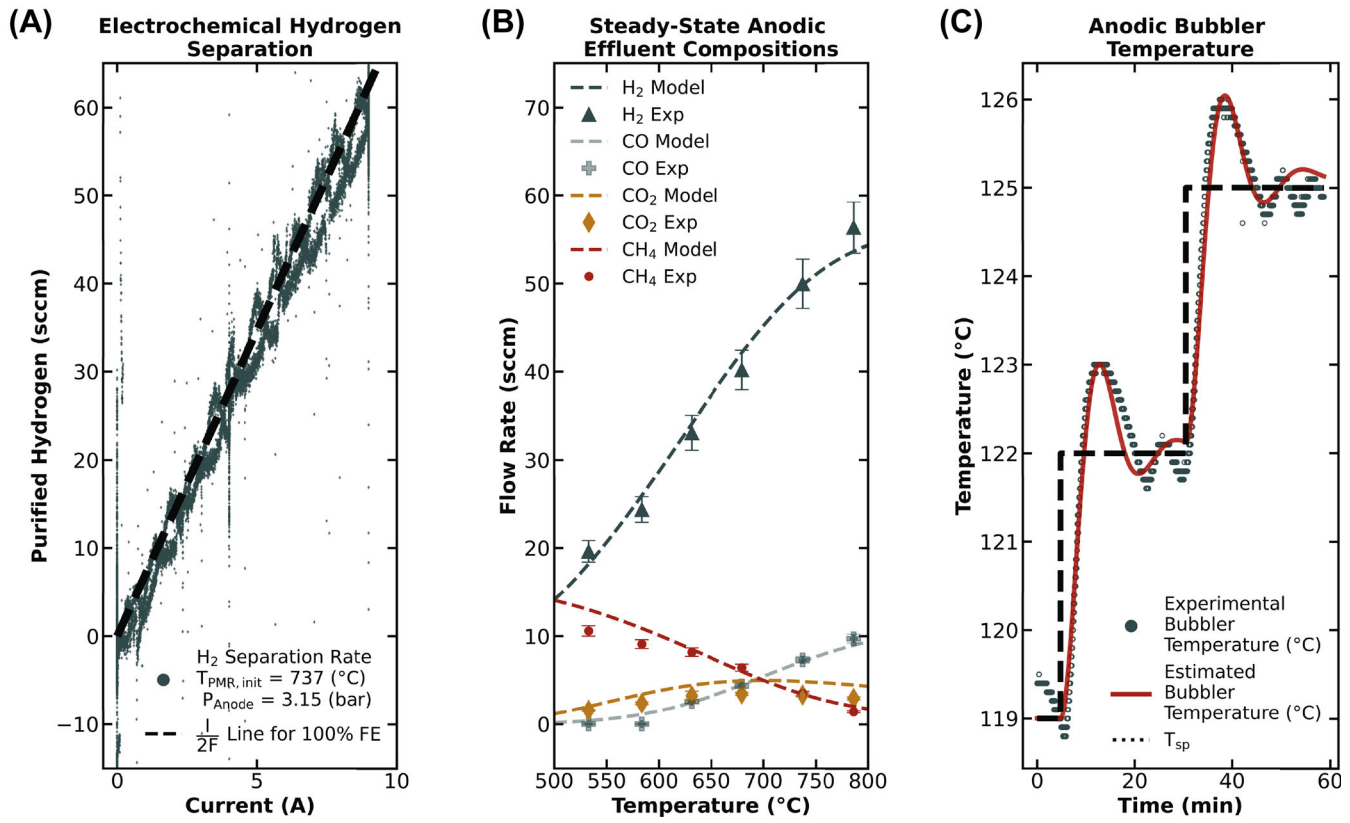

FIGURE 7 Experimental validation of all three process models to be used for state estimation in the DMPC algorithms. (A) Hydrogen purification as a function of applied electric current at a sweep rate of 8.00×10^{-3} A·(5 s)$^{-1}$, (B) Steady-state anodic gas compositions in the absence of electrochemical separation, and (C) Bubbler temperature response to changes in the PD-controller setpoint T_{sp}.

As discussed in Section 2.5, a second-order response model is used to simulate the dynamic behavior of the bubbler temperature dynamics in response to manipulated PD-control inputs. The parameters of the second-order bubbler model are tuned to match the experimental data from the open-loop bubbler experiments in Figure 6C. In the open-loop experiment, the setpoint of the bubbler temperature $T_{b,sp}$ is changed from 119°C to 122°C, and from 122°C to 125°C under 3.15 bar of pressure. An underdamped response of bubbler temperature is observed, indicating $0<\zeta_b<1$. In a second-order response system, maximum overshoot M_p, decay ratio DR between successive peaks, period of damped oscillation T_d, and rise time T_r are four key dynamic characteristics, which are defined as follows:

$$M_p = e^{-\frac{\pi\zeta_b}{\sqrt{1-\zeta_b^2}}},\quad DR = e^{-\frac{2\pi\zeta_b}{\sqrt{1-\zeta_b^2}}},\quad T_d = \frac{2\pi\tau_b}{\sqrt{1-\zeta_b^2}},\quad T_r \approx \frac{\pi-\arccos(\zeta_b)}{\frac{1}{\tau_b}\sqrt{1-\zeta_b^2}} \tag{36}$$

Based on Equation (36), the estimated values of M_p, DR, T_d and T_r are 30.9%, 9.56%, 15.8 min and 4.88 min, which aligns with experimental observations (33.0%, 10.0%, 13.0 min and 4.35 min, for all Equation (36) constants, respectively). The mean absolute error of the model is 0.19°C. Hence, the results demonstrate the reliability of Equation (36) in predicting the anodic bubbler dynamics over the operational domain of the PMR system.

4.3 | Simulation validation and comparison

If the disturbance observer-based state estimator accurately forecasts offline controller input data from a PI control experiment, the convergence of the DMPC optimization algorithms is likely to result in converged solutions over each horizon and sampling step that minimize setpoint deviations and controller input efforts. To validate the state estimator, a test dataset was taken from a multi-input multi-output PI control scenario with initial values for the applied electric current I_0, feed methane flow rate $q_{CH_4,0}$, and PD-temperature setpoint $T_{sp,0}$ initialized to 0.00 A, 16.2 sccm, and 120°C, respectively. The total hydrogen production setpoints were 150 sccm and 125 sccm, to force dynamic operation of the PMR system. Likewise, the automatic setpoint generator was set to a 75% hydrogen recovery rate at a steam-to-carbon ratio of 3.30. The dynamic operation of the PMR system, along with the impulse changes in the applied electric current, which was an artifact of PI control action, was used to test the accuracy of the state estimator under the stress of uncertain control inputs and stochastic process disturbances. The results of this experimental

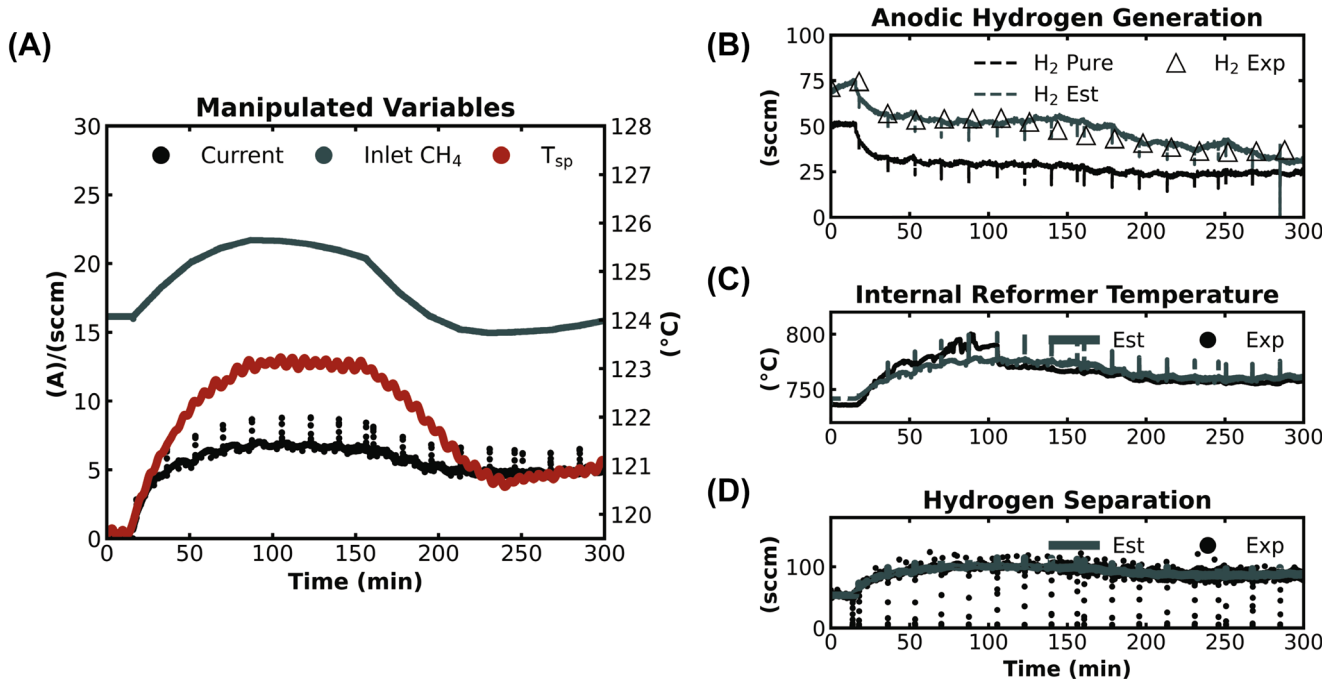

FIGURE 8 Offline test of state estimation using: (A) PI control inputs to estimate, (B) the anodic hydrogen generation rate as predicted by the pure model and state estimator, (C) the anode chamber energy balance, and (D) electrochemical hydrogen separation. In (A), the left y-axis units are A (current) or sccm (inlet CH4).

effort were used to determine the degree of robustness of the hybrid state estimation methodology of Section 3.3.

A comparison of the average errors of the state estimations relative to the actual values of the process is provided in Figure 8. Under dynamic operation, hydrogen predictions in both the anode and cathode chambers of the reformer unit are sufficiently accurate. Specifically, the average absolute errors are less than 3.50 sccm for both target variables. More importantly, the offline 0.50 to 2.00 A step changes in the applied electric current, due to PI control actions, do not proliferate estimation errors, which proves the power of the disturbance observer-based state estimation design. Robust estimations of the reformer temperature were also observed, evidenced by an average absolute error of 5.65°C. Additionally, the offline dynamic model validation exercise confirms that the PMR energy balance (Equation 12) accurately predicts the temperature of the anode chamber in the PMR unit.

5 | EXPERIMENTAL MPC RESULTS

5.1 | Decentralized MPC

In the first control scenario S1 (Figure 9), the system-wide hydrogen flow rate was set to 150 sccm, and the hydrogen purification rate (hydrogen recovery) was set to 75.0% of the total system-wide hydrogen flow rate at t_{-900s}. To ensure adequate hydration of the protonic membrane during enhanced water vapor consumption—at higher reaction rates—the S/C ratio was changed to 3.30 at the initial control time. Hydrogen separation rates were calculated from real-time feedback from the digital mass flow meter, following the automation algorithm developed in Alg. 1. DMPC 1 also stabilized around the adaptive purification rate setpoint with an average absolute error of 6.15 sccm. A maximum applied electric current of 9.47 A was achieved for DMPC 1 to increase the forward rates of the equilibrium SMR reactions by removing hydrogen product from the reaction zone. The average DMPC 2 error for $(y_{2,sp} - y_2)$ was 10.55 ±5.78 sccm, which had a settling time of approximately 197 min to ±5% of $y_{2,sp}$ and a methane feed range of 16.2 to 31.1 sccm. DMPC 3 settled to ±5% of $y_{3,sp}$ after 83 min with an average error of 0.284 ±0.185 sccm throughout the control time. Figure 10 displays results from the second control scenario S2 with DMPC 1 automatic setpoint generation set to 90% of the total hydrogen in the system at t_{-900s}. The second and third closed-loops maintained the setpoints from the first control scenario S1: 150 sccm for the total hydrogen generation rate and a steam-to-carbon ratio of 3.30. DMPC 1, via the modification of the automatic setpoint calculation, drove y_1 to higher average hydrogen purification rates that fully utilized the explicit input constraint on u_1 to protect the protonic membrane from rapid Joule-heating (Figure 10). The maximum separation rate for control scenario S2 was 76.9 sccm, leading to a maximum hydrogen recovery rate of 84.4% and an average hydrogen recovery rate of 68.7% throughout the control time (234 min).

5.2 | Comparison with classical control

The classical control results of Peters et al.[18] provide a standard for comparison when evaluating the effectiveness of the DMPC control

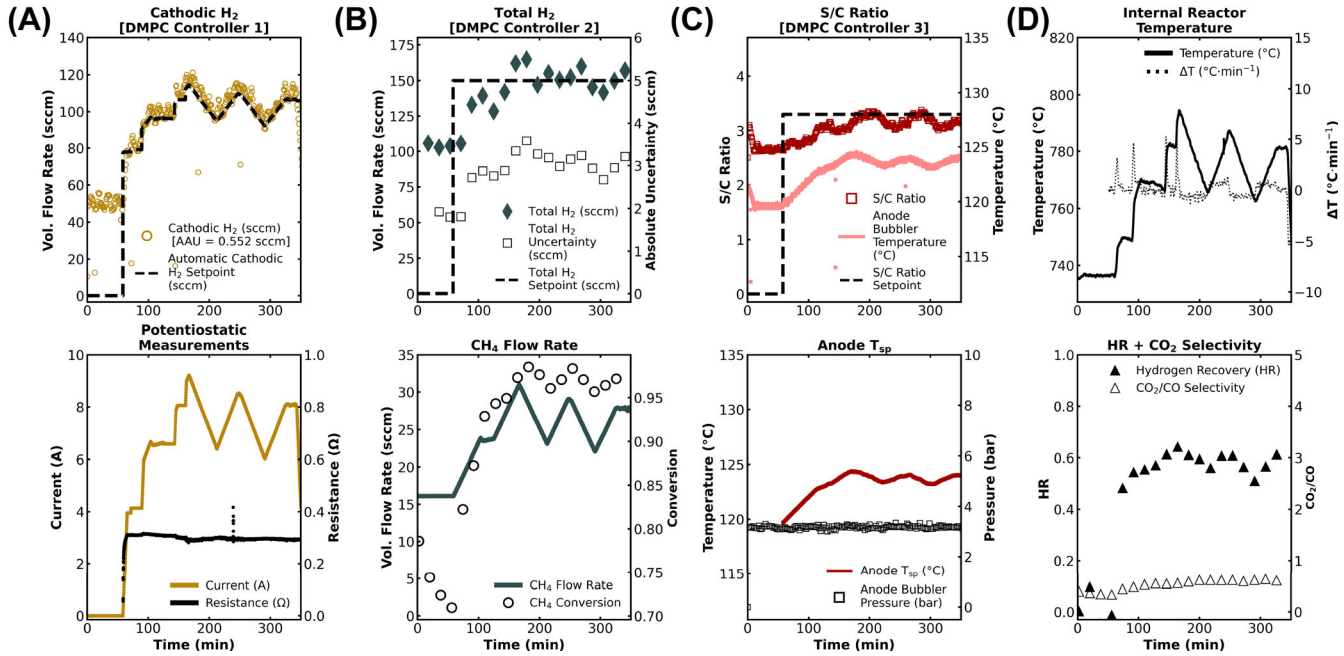

FIGURE 9 DMPC scenario S1 results for a total H_2 setpoint of 150 sccm ($T_0 = 737°C$ | $I_0 = 0.00$ A | $q_{CH_4,0} = 16.2$ sccm | $T_{sp,0} = 120°C$). (A)–(C) Control loops for electrochemical hydrogen separation, overall hydrogen production, and the feed steam-to-carbon ratio, respectively. The average absolute uncertainty (AAU) for Controller 1 is an average of flow meter uncertainties throughout the control experiment (Alicat mass flow meter absolute uncertainty was ±0.6% of flow reading). (D) Subplots for the internal temperature of the PMR unit, system hydrogen recovery, and carbon oxide by-product selectivity.

FIGURE 10 DMPC scenario S2 results for a total H_2 setpoint of 150 sccm ($T_0 = 737°C$ | $I_0 = 0.00$ A | $q_{CH_4,0} = 16.2$ sccm | $T_{sp,0} = 120°C$). (A) Control loop for electrochemical hydrogen separation, (B) Subplots for the internal temperature of the PMR unit, system hydrogen recovery, and carbon oxide by-product selectivity.

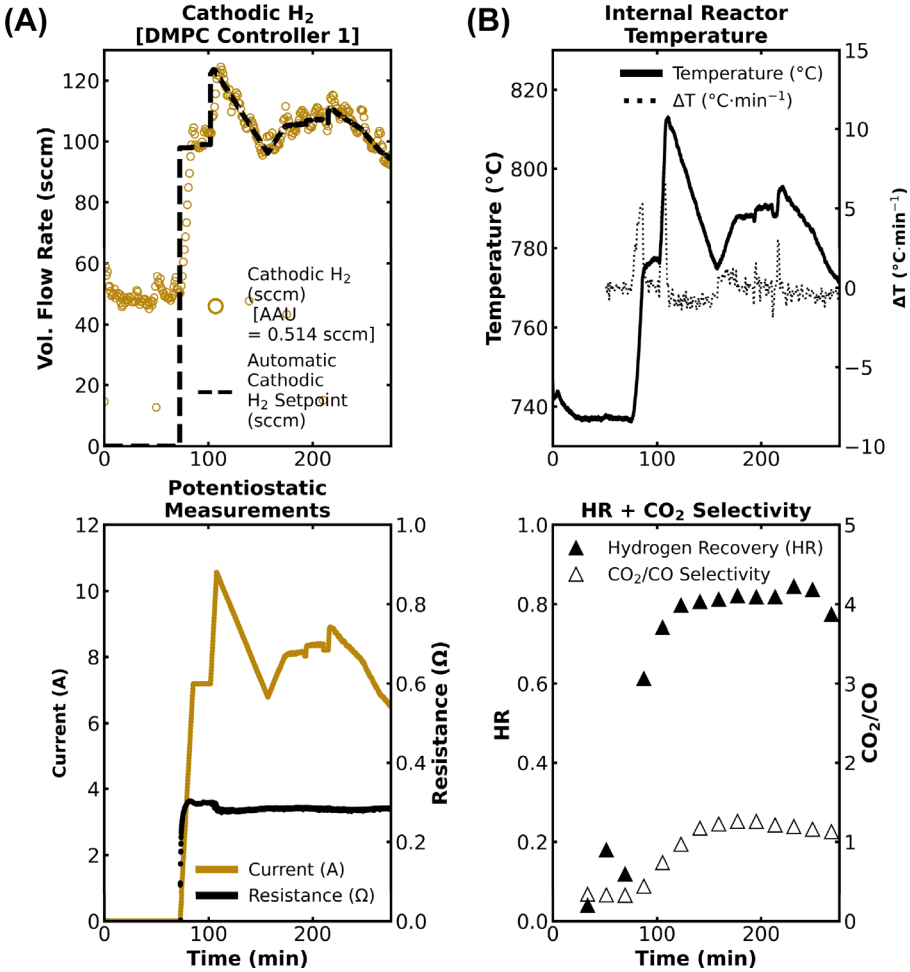

TABLE 3 Comparison of control performance metrics for PI and DMPC for three feedback loops.

Metric	H_2 Purification	H_2 Generation	S/C ratio
PI			
AAE	5.15 sccm	7.42 sccm	0.14
Settling Time (min)	14.5	108	31.5
Control Smoothness Effort	1.4×10^2 $A^2 \cdot s$	1.7×10^2 $sccm^2 \cdot s$	1.4×10^4 $^\circ C^2 \cdot s$
DMPC			
AAE	6.15 sccm	10.6 sccm	0.28
Settling Time (min)	13.5	162	83.2
Control Smoothness Effort	2.6 $A^2 \cdot s$	1.8 $sccm^2 \cdot s$	1.4×10^4 $^\circ C^2 \cdot s$

Note: All controller tuning methods and parameters for the classical control experiments can be found in the previous work of Peters et al.[18] The settling time is determined after 1 h of consecutive feedback samples within ±10% of the target setpoints. Control smoothness effort is calculated using the following integral approximation: $\sum_{k=k_0+1}^{k_f} (u_k - u_{k-1})^2 \cdot \Delta t$.

architecture developed in this work. Table 3 provides results for setpoint tracking and compares the performance of the classical and predictive control methodologies for all three control loops. The overall DMPC design excels at minimizing the effort to maintain control action smoothness for each manipulated input, which is essential to avoid protonic membrane damage when applied electric currents are actuated. Further, the settling time for DMPC 1 outperforms that of PI 1 by 1.00 min. For control loops two and three, the results are more nuanced. While the control smoothness effort is less for DMPC 2, the settling time and average absolute error for PI controllers two and three are superior. Specifically, the classical controllers for the second and third feedback loops settle at the target hydrogen production and S/C ratio setpoints 33.3% and 164% faster, respectively, as compared to DMPC 2 and DMPC 3 throughout the respective control times. Additionally, the average absolute errors for all PI closed-loops are lower than the absolute average errors of the DMPC control scheme for both control scenarios.

5.3 | Optimizer performance

All computational solutions in the decentralized predictive controllers for control scenarios S1 and S2 have a 98% convergence rate. In fact, DMPC 3 converged for all sample steps during S1 and S2, and DMPC 1 also had perfect convergence for all sample steps in S2. DMPC 1 did not converge for 21 sample steps throughout the control time of S1. The solution failures can be attributed to instantaneous changes in cathodic flow rate due to pressure oscillations that blocked the back pressure regulator valve, as evidenced by rapid dips in the cathodic flow rate in Figure 9. Another important metric for the successful implementation of experimental decentralized controllers is the optimization solution time per controller sampling step. Figure 11 provides the logarithmic distributions of each optimizer solution time for both control scenarios S1 and S2. The average control action calculation times for DMPC 1, DMPC 2, and DMPC 3 were 2.7 $\times 10^{-2}$ s, 2.7 $\times 10^{-1}$ s, and 2.7 $\times 10^{-2}$ s, respectively. A maximum solution time of 4.6 s was seen for the DMPC 2 solution, falling within the 5-second controller sampling window. During the control experiment under S2 conditions, the average control action calculation times for two of the three predictive controllers were greater than those for the S1 calculation time. The average calculation times for the first and second decentralized controllers during S2 were 2.8 $\times 10^{-2}$ s and 3.1 $\times 10^{-1}$ s, respectively, while the calculation time for controller three remained the same as for control scenario S1.

6 | ANALYSIS OF EXPERIMENTAL RESULTS

Review of the control objectives listed in Section 3.2 provides the primary evaluation criteria for the multi-input multi-output DMPC architecture. Throughout the three experiments for control scenario S1, and two experiments for control scenario S2, all control loops maintained safe PMR operating conditions and did not cause reactor or system damage. Complete hydrogen depletion in the protonic membrane was also averted, given the successful implementation of the dynamic setpoint compensation algorithm for DMPC 1, further evidenced by the lack of voltage spikes throughout control times (Figure 9B; Figure 10B). Likewise, the controllers were able to reach all three target setpoints reproducibly for both control scenarios, showing the success of the disturbance-based state observer in forecasting system states in the presence of experimental catalyst deactivation, pressure oscillations, and variable magnitudes of Joule-heating. For DMPC 1, an explicit control input constraint to limit the discrete change in the applied electric current between sampling steps was also satisfied in both control scenarios. However, the control input limits still led to actuated electric currents that produced two instances of the discrete reformer temperature derivative exceeding $\pm 5^\circ C \cdot min^{-1}$. The maximum reformer temperature change rate was $5.27^\circ C \cdot min^{-1}$ during S1. During scenario S2, two instances of a $\pm 5^\circ C \cdot min^{-1}$ reformer temperature change were also recorded and were likely the result of increased membrane electrical resistance during the initial DMPC 1 electric current ramps from 0.00 to 7.00 A. Although the constraint on u_1 can be further modified, the fact that

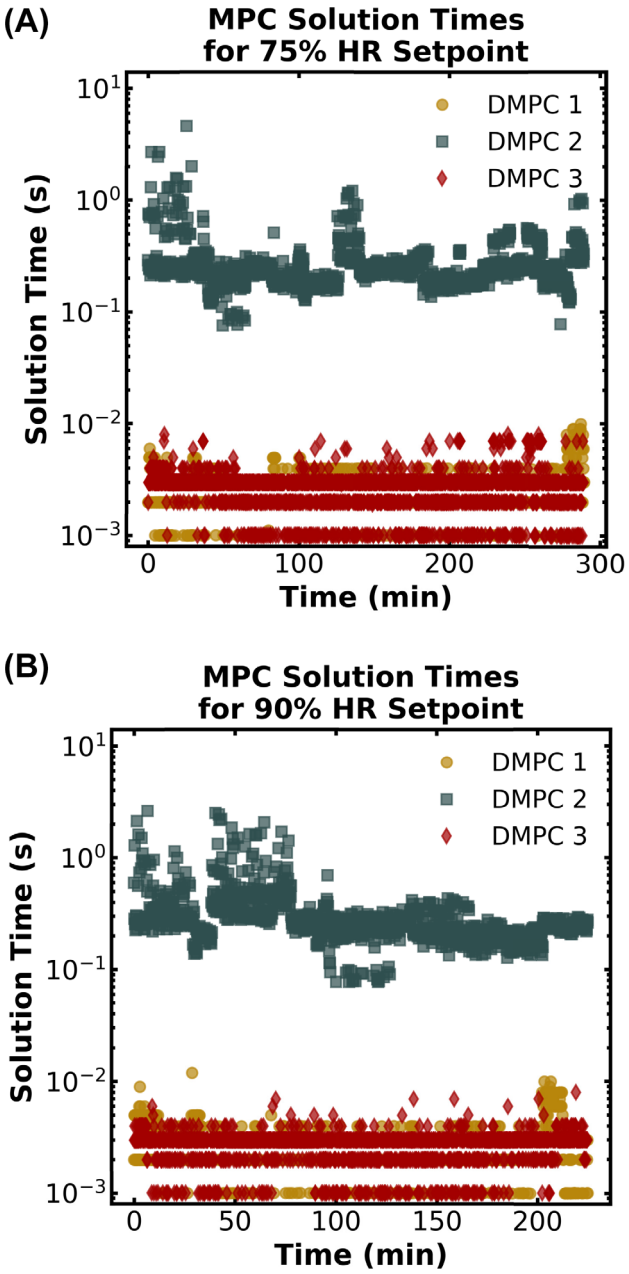

FIGURE 11 DMPC solution times per sampling step for all three input-output variable pairings. (A) Optimizer solution times for control scenario S1, (B) Optimizer solution times for control scenario S2.

the reformer temperature dynamics stayed within $\pm 5^{\circ}C \cdot min^{-1}$ for over 99% of the control times in S1 and S2 proves that the DMPC 1 regulator adequately protects the protonic membrane from rapid Joule-heating (Figure 10).

The error between the reaction separation term $\frac{I_m}{2F}$ and the observed separation rate was limited to less than 4.00 sccm (Figure 7A). However, when addressing the results of DMPC 2 and DMPC 3, there are obvious oscillations around the setpoint during tracking that can be improved by changing the sampling rate of the DMPC 2 sensor. Specifically, the GC takes measurements of the anodic product gas composition once every 18.0 min with a 15.0 min time delay, which limits the effectiveness of the disturbance observer. In future studies, the GC will be replaced with infrared detectors that have sampling rates of around one second to eliminate sensor delay and infrequent feedback. For DMPC 3, the main source of the setpoint oscillations during tracking originated from small deviations ($\leq 1^{\circ}C$) in T_b from the target $T_{b,sp}$ and had a substantial impact on the real-time steam-to-carbon ratio calculations. A direct connection between the electrical heating tape of the bubbler and the DMPC 3 controller is suggested, as removing the secondary PD-controller would likely decrease the order of the anodic bubbler dynamic response.

Most importantly, the use of a decentralized predictive controller to regulate the hydrogen purification rate in PMR systems is supported by the control results from scenarios S1 and S2 that show smoother and more reliable control actions, enhancing the electrochemical performance of the protonic membrane. As a consequence, the protonic membrane was pushed to higher current densities (0.69 $A \cdot cm^{-2}$) and achieved over 84% hydrogen recovery, compared to a maximum of only 50.4% recovery for the classical control case. So, while disturbances such as catalytic activity variation and bubbler pressure oscillations decreased the settling times of the second and third control loops of the DMPC architecture, more hydrogen can be purified by using a predictive controller on the first feedback loop to enhance the economic viability of the process. The computational reliability of the optimization algorithms prevented ineffective or dangerous control action calculations in the real system and also satisfied all computational performance control objectives. Furthermore, the computational performance results signify that the validated dynamic models are sufficiently predictive and yet computationally inexpensive for real-time implementation of the control architecture.

7 | CONCLUSION

The experimental implementation of a decentralized model predictive control architecture was carried out as a potential automation pathway for protonic membrane reforming systems. Validated dynamic models for steam and hydrogen generation, along with hydrogen purification, were fit to match the residence times, dead times, anodic gas phase compositions, anodic energy distribution, and hydrogen purification rates of the experimental process. A unique state observer framework for a nonlinear disturbance observer provided robust state estimation for all three predictive controllers for control scenarios S1 and S2 with different hydrogen purification rate settings. Judged based on control robustness, stability, settling times, and economic value, the study demonstrates that the additional complexity of using model predictive control for the electric current and hydrogen separation variable pairing is justified and recommended. Additional variable couplings related to product selectivity may also be considered in future work. For example, changing the furnace temperature or the system pressure directly changes the selectivity of carbon dioxide to carbon monoxide, which further determines how much hydrogen can be produced and the composition of the process by-product.

In conclusion, this work as a whole provides a proof of concept for the first experimental implementation of three model predictive controllers for membrane reformers or proton exchange membranes. Chief among all findings is the observation of hydrogen recovery rates exceeding 84% with the enhanced ability to set higher separation rate setpoints when the PMR unit and potentiostat are protected by an explicit constraint on the applied electric current. Thus, control engineers may think to employ predictive control for hydrogen regulation and perhaps use classical methods for hydrogen and steam generation rates when developing control systems for protonic membrane reforming systems.

AUTHOR CONTRIBUTIONS

Dominic Peters: Writing—original draft; methodology; investigation; conceptualization. **Xiaodong Cui**: Writing—original draft; methodology; investigation; conceptualization. **Yifei Wang**: Methodology; conceptualization. **Carlos G. Morales-Guio**: Writing—original draft; supervision; funding acquisition; conceptualization. **Panagiotis D. Christofides**: Writing—original draft; supervision; funding acquisition; conceptualization.

ACKNOWLEDGMENT

The authors gratefully acknowledge financial support from the U.S. Department of Energy, through the Office of Energy Efficiency and Renewable Energy (EERE), under the Advanced Manufacturing Office Award Number DE-EE0007613. The authors also express sincere gratitude to CoorsTek, Inc., for providing the BZCY proton-conducting membranes used to construct the protonic membrane reformer unit.

DATA AVAILABILITY STATEMENT

The data that support the findings of this study are available on request from the corresponding author. The data are not publicly available due to privacy or ethical restrictions.

All dynamic models and the associated frameworks for calculating key process variables are provided in Sections 2 and 3. Numerical data from experimental sensors and real-time LabVIEW calculations are provided for Figures 6–11. The experimental data are tabulated in the Supplementary Material. All sensor measurements and LabVIEW calculations provide information about the evolution of the PMR system states as a function of time, temperature, pressure, feed compositions, and control decisions.

ORCID

Panagiotis D. Christofides https://orcid.org/0000-0002-8772-4348

REFERENCES

1. Le TT, Sharma P, Bora BJ, et al. Fueling the future: A comprehensive review of hydrogen energy systems and their challenges. *Int J Hydrog Energy*. 2024;54:791-816.
2. McKinsey & Company. *Tackling Heat Electrification to Decarbonize Industry*. McKinsey & Company; 2024.
3. Fjeld H, Clark D, Yuste-Tirados I, et al. Thermo-electrochemical production of compressed hydrogen from methane with near-zero energy loss. *Nat Energy*. 2017;2:923-931.
4. Christofides PD, Daoutidis P. Robust control of multivariable two-time-scale nonlinear systems. *J Process Control*. 1997;7:313-328.
5. Lin ST, Chen YH, Yu CC, Liu YC, Lee CH. Dynamic modeling and control structure design of an experimental fuel processor. *Int J Hydrog Energy*. 2006;31:413-426.
6. Malik FR, Tieqing Z, Kim YB. Temperature and hydrogen flow rate controls of diesel autothermal reformer for 3.6 kW PEM fuel cell system with autoignition delay time analysis. *Int J Hydrog Energy*. 2020;45:29345-29355.
7. Cifuentes A, Serra M, Torres R, Llorca J. Experimental control of a methanol catalytic membrane reformer. *Reactions*. 2023;4:702-712.
8. Andreasen SJ, Kær SK, Sahlin S. Control and experimental characterization of a methanol reformer for a 350 W high temperature polymer electrolyte membrane fuel cell system. *Int J Hydrog Energy*. 2013;38:1676-1684.
9. Li G, Fu H, Madonski R, et al. Feed-forward offset-free model predictive temperature control for proton exchange membrane fuel cell: An experimental study. *ISA Trans*. 2022;128:159-170.
10. Çitmaci B, Peters D, Cui X, et al. Feedback control of an experimental electrically-heated steam methane reformer. *Chem Eng Res Des*. 2024;206:469-488.
11. Anwar MF, Yu Y, Khalid M, et al. Electrochemical insights into performance enhancement of protonic ceramic fuel cells with Ba(Zr,Ce,Y)$O_{3-\delta}$ electrolyte. *Energy Mater*. 2025;5(8):500102.
12. Su H, Hu YH. Degradation issues and stabilization strategies of protonic ceramic electrolysis cells for steam electrolysis. *Energy Sci Eng*. 2021;10(5):1706-1725.
13. Sariyildiz E. Disturbance observer-based robust control and its applications 35th anniversary overview. *IEEE Trans Ind Electron*. 2022;67(3):2042-2053.
14. Cui X, Peters D, Wang Y, et al. Modeling and control of a protonic membrane steam methane reformer. *Chem Eng Res Des*. 2024;212:493-519.
15. Moore T, Wong A, Giera B, et al. Accelerating climate technologies through the science of scale-up. *Nat Chem Eng*. 2024;1(12):731-740.
16. Luterbacher J, Weckhuysen B, Haussener S, et al. Connecting scales in reaction engineering. *Nat Chem Eng*. 2025;2:156-159.
17. Yuste-Tirados I, Liu X, Kjølseth C, Norby T. Impedance of a tubular electrochemical cell with BZCY electrolyte and Ni-BZCY cermet electrodes for proton ceramic membrane reactors. *Int J Hydrog Energy*. 2023;48:30027-30038.
18. Peters D, Cui X, Wang Y, et al. Automation and control of an experimental protonic membrane steam methane reforming system. *Digit Chem Eng*. 2025;15:100240.
19. Maslar JE, Kimes WA, Sperling BA, Kanjolia RK. Characterization of bubbler performance for low-volatility liquid precursor delivery. *J Vac Sci Technol A*. 2019;37:041506.
20. Froment GF, Bischoff KB, et al. *Chemical Reactor Analysis and Design*. 3rd ed. John Wiley & Sons; 2010.
21. Schmidt L. *Chemical Reaction Engineering*. 3rd ed. Wiley; 2005.
22. Xu J, Froment GF. Methane steam reforming, methanation and water-gas shift: I. Intrinsic kinetics. *AICHE J*. 1989;35:88-96.
23. Wrubel JA, Gifford J, Ma Z, Ding H, Ding D, Zhu T. Modeling the performance and faradaic efficiency of solid oxide electrolysis cells using doped barium zirconate perovskite electrolytes. *Int J Hydrog Energy*. 2021;46:11511-11522.
24. Cui X, Çitmaci B, Peters D, et al. Estimation-based model predictive control of an electrically-heated steam methane reforming process. *Digit Chem Eng*. 2024;11:100153.
25. Chen WH, Yang J, Guo L, Li S. Disturbance-observer-based control and related methods—An overview. *IEEE Trans Ind Electron*. 2015;63:1083-1095.

26. Johnson C. Further study of the linear regulator with disturbances–The case of vector disturbances satisfying a linear differential equation. *IEEE Trans Autom Control*. 1970;15:222-228.
27. Chen J, Patton RJ, Zhang HY. Design of unknown input observers and robust fault detection filters. *Int J Control*. 1996;63:85-105.
28. Maeder U, Borrelli F, Morari M. Linear offset-free model predictive control. *Automatica*. 2009;45:2214-2222.
29. Wang Y, Cui X, Peters D, et al. Machine learning-based predictive control of an electrically-heated steam methane reforming process. *Digit Chem Eng*. 2024;12:100173.
30. Wallace M, Pon Kumar SS, Mhaskar P. Offset-free model predictive control with explicit performance specification. *Ind Eng Chem Res*. 2016;55:995-1003.
31. Pannocchia G, Gabiccini M, Artoni A. Offset-free MPC explained: Novelties, subtleties, and applications. *IFAC-PapersOnLine*. 2015;48:342-351.
32. Pannocchia G. Offset-free tracking MPC: A tutorial review and comparison of different formulations. *Proceedings of European Control Conference*. IEEE; 2015:527-532.
33. Nascimento C, Alves V, Harun NF, et al. Identification of control state changes in a power plant desuper heater system via transfer functions and Gaussian process modeling. *Proceedings of ASME Power Conference*. ASME; 2024:V001T05A009.
34. Chen H, Lou S, Lv C. Hybrid physics-data-driven online modelling: Framework, methodology and application to electric vehicles. *Mech Syst Signal Process*. 2023;185:109791.
35. Champaney V, Chinesta F, Cueto E. Engineering empowered by physics-based and data-driven hybrid models: A methodological overview. *Int J Mater Form*. 2022;15:31.
36. Kasilingam S, Yang R, Singh SK, Farahani MA, Rai R, Wuest T. Physics-based and data-driven hybrid modeling in manufacturing: A review. *Prod Manuf Res*. 2024;12:2305358.

SUPPORTING INFORMATION

Additional supporting information can be found online in the Supporting Information section at the end of this article.

How to cite this article: Peters D, Cui X, Wang Y, Morales-Guio CG, Christofides PD. Model predictive control of an experimental protonic membrane steam methane reforming system. *AIChE J*. 2026;72(2):e70105. doi:10.1002/aic.70105